# Targeting Slc7a11 improves efferocytosis by dendritic cells and diabetic wound healing

Sophia Maschalidi[1,2†], *Parul Mehrotra[1,2], *Burcu N. Keçeli[1,2], Hannah K.L. De Cleene[1,2], Kim Lecomte[2,3], Renée Van der Cruyssen[2,4], Pauline Janssen[5], Jonathan Pinney[6,7], Geert van Loo[2,3], Dirk Elewaut[2,4], Ann Massie[5], Esther Hoste[2,3], Kodi S. Ravichandran[1,2,6,7,8†]

* Contributed equally; † Corresponding authors

[1]*Unit for Cell Clearance in Health and Disease, VIB Center for Inflammation Research, Ghent, Belgium;*

[2]*Department of Biomedical Molecular Biology, Ghent University, Ghent, Belgium;*

[3]*Unit for Cellular and Molecular Pathophysiology, VIB Center for Inflammation Research, Ghent, Belgium;*

[4]*Laboratory for Molecular Immunology and Inflammation, Department of Rheumatology, Ghent University Hospital, Ghent, Belgium;*

[5]*Laboratory of Neuro-Aging & Viro-Immunotherapy, Center for Neurosciences (C4N), Vrije Universiteit Brussel, Brussels, Belgium;*

[6]*The Center for Cell Clearance, University of Virginia, Charlottesville, VA, USA;*

[7]*Department of Microbiology, Immunology, and Cancer Biology, and the Center for Cell Clearance, University of Virginia, Charlottesville, VA, and*

[8]*Division of Immunobiology, Department of Pathology and Immunology, Washington University School of Medicine, St. Louis, MO, USA.*

**Chronic non-healing wounds are a major complication of diabetes, which impacts 1 in 10 people worldwide. Dying cells in the wound perpetuate the inflammation and contribute to dysregulated tissue repair[1-3]. Here, we reveal the membrane transporter Slc7a11 as a molecular 'brake' on efferocytosis, the process by which dying cells are removed, and that inhibiting Slc7a11 can accelerate wound healing. First, transcriptomics of efferocytic dendritic cells identified upregulation of several *Slc7* gene family members. In further analyses, pharmacological inhibition, siRNA knockdown, or deletion of *Slc7a11* enhanced dendritic cell efferocytosis. Interestingly, *Slc7a11* was highly expressed in skin dendritic cells, and scRNAseq of inflamed skin showed *Slc7a11* upregulation in innate immune cells. In a mouse model of excisional skin wounding, loss of Slc7a11 expression or inhibition accelerated healing dynamics and reduced apoptotic cell load in the wound. Mechanistic studies revealed a link between Slc7a11, glucose homeostasis, and diabetes. Slc7a11-deficient dendritic cells relied on glycogen store-derived aerobic glycolysis for improved efferocytosis, and transcriptomics of efferocytic Slc7a11-deficient dendritic cells identified genes linked to gluconeogenesis and diabetes. Further, *Slc7a11* expression was higher in the wounds of diabetic-prone *db/db* mice, and targeting Slc7a11 accelerated their wound healing. The faster healing was also linked to the release of TGF-β family member GDF15 from efferocytic dendritic cells. Collectively, Slc7a11 is a negative regulator of efferocytosis, and removing this brake improves wound healing, with significant implications for diabetic wound management.**

**MAIN**

Billions of cells in the body are turned over via apoptosis on a daily basis. These are then recognized and removed by phagocytes via the process of 'efferocytosis'[1]. Defects in efferocytosis is associated with non-resolving inflammation leading to chronic inflammatory conditions[2,3]. Dendritic cells are a heterogenous group of phagocytes in nearly all tissues. Dendritic cells display multiple phagocytic and pathogen recognition receptors and help maintain tissue homeostasis through regulation of innate and adaptive immunity[4]. While apoptotic cell uptake by dendritic cells has long been recognized, this has primarily been studied in the context of the antigen presentation and adaptive immunity[5,6,7,8]. Compared to macrophages, much less is known about molecular regulation of dendritic cell efferocytosis and its relevance to limiting inflammation.

As the body's largest organ, our skin acts as a barrier to protect internal tissues from extreme temperature, water loss, ultraviolet radiation, microbial and chemical insults, and injury. Tissue repair after skin injury involves clearance of apoptotic cells by phagocytes at the wound site as part of resolving the inflammation and restoring the barrier[9,10]. Chronic non-healing wounds, such as those associated with diabetes, aging, or vascular disease, severely affect the quality of life including risks for infection[11]. Homeostasis in healthy skin is maintained by immune cells including dendritic cells, macrophages, and T cells populating the tissue. Langerhans cells (LCs) residing in the epidermis, together with dendritic cells in the dermis maintain surveillance by capturing dead cells or pathogens and presenting them to effector T cells[12,13]. Resident or recruited macrophages[14,15] and neutrophils[16] have been both positively and negatively linked to wound healing dynamics; however, the contribution of dendritic cells to injury repair is less defined. In this work, while characterizing gene programs in dendritic cells engulfing apoptotic cells, we serendipitously discover the plasma membrane protein Slc7a11 as a novel brake on dendritic cell-mediated efferocytosis and reveal its relevance to cutaneous wound healing.

## Upregulation of amino acid transporters in dendritic cells engulfing apoptotic cells

To define gene signatures initiated in dendritic cells during efferocytosis, we incubated primary mouse bone-marrow dendritic cells (BMDC phagocytes) with labeled apoptotic human Jurkat cells, purified the engulfing dendritic cells, and performed RNAseq analysis (Fig. 1a). We used this cross-species approach to distinguish the mouse DC-derived RNA from apoptotic cargo-derived human RNA. We also used plain beads as targets to

control for phagocytosis. In our analysis, we focused on differentially expressed genes associated with 'transporter' activity based on the initial hypothesis that dendritic cells may have molecular features that differ from other phagocytes. We found significant alterations in genes encoding membrane transporters with diverse functionalities including those that passage ions, lipids, and amino acids (Fig. 1b). Interestingly, the solute carrier (Slc) family of genes represented 29% of the differentially expressed transporters in efferocytic dendritic cells (Fig. 1c). SLCs represent the second largest gene family in the human genome (after the GPCRs), and mediate transport of metabolites and solutes across cellular membranes. SLCs are also linked to >100 human diseases and implicated in efferocytosis by other phagocytes[17] (Fig. 1c). In efferocytic dendritic cells, *Slc* genes coding for amino acid metabolism and carbohydrate catabolism were upregulated, while *Slc* genes linked to oxidative phosphorylation (OXPHOS) and fatty acid transport were downregulated (Extended data 1a).

Amino acid transport is fundamental for nutrient supply and supports key functions of immune cells[18,19], including dendritic cells[20]. Thus, we examined cationic (Slc7a1through Slc7a4) and hetero(di)meric amino acid transporters (Slc7a5 through Slc7a11), as well as Slc3a2, which helps to chaperone/facilitate localization of some Slc7 members[21]. Efferocytic dendritic cells had the greatest increase in *Slc7a5* and *Slc7a11* (Fig. 1d).

## Slc7a11 antiporter acts as a brake for efferocytosis by dendritic cells

To test the relevance of these Slc7 family amino acid transporters, we performed siRNA-mediated knockdown in BMDC, followed by efferocytosis via both a flow cytometry-based assay and live cell imaging. Interfering with *Slc7a11* expression consistently led to greater efferocytosis by dendritic cells (Fig. 1e). Slc7a11, also referred as xCT, is the subunit of the cysteine-glutamate antiporter system $x_c^-$ that regulates exchange of intracellular glutamate for extracellular cysteine, the latter being a rate-limiting precursor for synthesis of the antioxidant glutathione (GSH). Slc7a11 is also linked to neurological diseases[22-26], viral infections[27-29] and cancers[30,31], with drugs targeting Slc7a11 tested in clinical trials. In our assays, knockdown or pharmacologic inhibition of *Slc7a5* only showed a trend toward more efferocytosis but was not statistically significant, while *Slc7a1* did not affect BMDC efferocytosis (Extended data 1b-e).

We were initially surprised that Slc7a11 acts as a negative regulator of efferocytosis, as its expression goes up robustly during efferocytosis. Therefore, we took additional pharmacological and genetic approaches. Inhibition of Slc7a11 with the drug erastin caused a

boost in efferocytosis (Fig. 1f); in contrast, erastin did not affect the phagocytosis of E. *coli* bioparticles by dendritic cells (Extended data 2a). Although erastin is a ferroptosis inducer in cancer cells[32-34], another ferroptosis-inducing compound, ML-162[32] did not enhance efferocytosis (Extended data 2b). Moreover, the antioxidant Ferrostatin-1[35], a potent inhibitor of ferroptosis, did not reverse the enhanced DC efferocytosis due to Slc7a11 inhibition (Extended data 2c). While erastin treatment did reduce intracellular glutathione (GSH) levels (Extended data 2d), it only modestly increased lipid ROS accumulation (Extended data 2f) and did not affect dendritic cell viability (Extended data 2e). When we assessed the contribution of GSH and ROS, neither supplementation nor depletion of GSH affected the enhanced efferocytosis of Slc7a11 knockout/inhibited dendritic cells (Extended data 3a, b). Ameliorating ROS with the compound FCCP or scavenging ROS with MitoTEMPO partially reversed the enhanced efferocytosis after Slc7a11 inhibition, although this effect was not statistically significant under the conditions tested. Thus, while Slc7a11 inhibition may have a ROS component for its effect, this is not sufficient to explain the enhanced efferocytosis (Extended data 3c, d). The effect of erastin was also mimicked by excess glutamate to 'block' the cysteine uptake via Slc7a11, although the glutamate effect was partial (Extended Fig. 2g) perhaps due to the lower Slc7a11 inhibition by glutamate compared to erastin[36]. On the other hand, addition of N-acetyl-cysteine (NAC), a synthetic precursor of cysteine, reversed the enhanced efferocytosis of erastin-treated DC (Extended Fig. 2h), suggesting that cysteine transport via Slc7a11 is an important component of the increased efferocytosis.

As a genetic approach, we compared purified primary splenic conventional dendritic cells from control and Slc7a11-deficient mice. We noted enhanced uptake by Slc7a11-deficient cDC1, but not cDC2. Similarly, *ex vivo* generated BMDC lacking Slc7a11 displayed greater efferocytosis (Fig. 1g, h, i). This effect was seen with apoptotic targets labelled with pH-insensitive (TAMRA) or pH-sensitive (CypHer5E) dyes (Fig. 1i), and was abrogated by blocking cytoskeletal rearrangement with cytochalasin D (Fig. 1h, i). The increased uptake scored in these assays was not due to defective digestion of apoptotic corpses, as control and Slc7a11-deficient dendritic cells showed similar degradation of CellTrace Violet labeled apoptotic cells (Extended data 1f). Further, there was no additive increase in efferocytosis of Slc7a11-deficient DCs treated with erastin, supporting the specificity for the erastin (Fig. 1h). Interestingly, neither peritoneal macrophages from WT mice treated with erastin nor BMDMs from Slc7a11-deficient mice displayed enhanced efferocytosis in these conditions (Extended data 1g-h). Lastly, the Slc7a11-deficient dendritic cells did not show an enhanced

uptake of 'live' cells (Fig. 1i). These data collectively suggest that Slc7a11 acts as brake on dendritic cell efferocytosis.

**Skin wound healing is accelerated in the context of Slc7a11 blockade**

As the continued presence of uncleared apoptotic cells is linked to chronic inflammation, we assessed gene expression profiles of SLCs in resident dendritic cell subsets in the spleen, lung, or the skin. Mining publicly available datasets (ImmGen) and comparing them via Tri-wise plots, *Slc7a11* gene is most highly expressed in skin-resident dendritic cells (Fig. 2a). In contrast, *Slc7a5* is more expressed in the spleen and lung DCs. Previous reports suggested that depletion of epidermal Langerin$^{+}$ cells enhances cutaneous wound healing[37], while depletion of dermal CD11c$^{+}$ DCs delays wound closure[38]. Thus, we addressed the link between Slc7a11 and dendritic cells during skin wound healing.

When we tested purified dermal dendritic cells isolated from the ears of Slc7a11-deficient mice, cDC1 cells showed enhanced efferocytosis; in comparison, Langerhans cells and cDC2 were poor engulfers *ex vivo* and their phagocytic capacity was unaltered by Slc7a11-deficiency (Fig. 2b, Extended data 4a). While CD64$^{pos}$ macrophages were potent at apoptotic cell uptake, Slc7a11 deficiency did not modify their uptake (Fig. 2b). Histology of wounded skin tissue showed Slc7a11 colocalizing with the DC marker CD11c (Fig. 2c), but not fibroblasts (Extended data 4b). Additionally, CD11c$^{+}$ DCs were proximal to and appeared to capture cleaved caspase-3$^{+}$ apoptotic corpses (Fig. 2d).

When we mined a human disease association database[39], *SLC7A11* associated most highly with skin diseases such as eczematoid dermatitis and recurrent skin infections (Extended data Table 1). Further, probing single-cell transcriptomics data from inflammatory skin lesions that develop into verrucous carcinomas (see Methods), we uncovered increased expression of *Slc7a11* in the innate immune cells (Fig. 2e), including several dendritic cell subsets (Extended data 4c-d). *Slc7a11* expression also increased in total skin lysates after full-thickness wounding, along with genes linked to wounding such as *Tgfb1* and *Tnf* (Fig. 2f).

Next, we tested whether interfering with Slc7a11 function may impact wound healing dynamics. We topically administered a metabolically stable and water-soluble version of erastin (called IKE)[40] to mice after full-thickness skin wounding (on day 0 to day 2). However, administering erastin alone did not improve wound healing (Extended data 4f). Based on prior work that efferocytic phagocytes could provide many beneficial factors to

dampen inflammation[2,3], we asked whether co-administering early stage apoptotic cells together with erastin might be of benefit. Remarkably, single administration of apoptotic cells to the wound site at day 0 along with erastin at day 0 and day 2 (referred to as 'erastin regimen' from here onwards) markedly accelerated wound healing (Fig. 2g, Extended data 4e), with faster and complete closure of initial wounds (Fig. 2h). Erastin-regimen-treated mice reached 50% wound closure at day 4, nearly 2 full days earlier than their respective controls (Fig. 2g). Importantly, administering apoptotic cells alone without erastin did not improve wound closure (Extended data 4f). Erastin regimen also greatly decreased the apoptotic cell burden in the wound with fewer cleaved caspase-3$^{+}$ cells (even after co-administering apoptotic cells) (Fig. 2i). Thus, the accelerated wound healing requires a bolus of early-stage apoptotic cells and Slc7a11 inhibition via erastin. This effect was not related to induction of ferroptosis in the skin, as a ferroptosis inducer RSL3[34] (given together with apoptotic cells) did not improve wound healing (Extended data 4g). Additionally, erastin regimen promoted keratinocyte migration at day 4 post-wounding without affecting proliferation of keratinocytes or fibroblasts (Extended data 4h, i, j). To test the erastin regimen on existing wounds, we administered erastin on day 2 to day 4 post-wounding, and this also led to faster healing (Fig. 2j).

To complement the above studies with a genetic approach, we tested Slc7a11KO mice (Fig. 2k), which also showed accelerated wound healing dynamics, and this also required co-administration of apoptotic cells on day 0 post-wounding. The wound closure in the Slc7a11-null mice also reached 50% of wound closure nearly 2 days earlier than the controls (Fig. 2g and 2k). Thus, interfering with Slc7a11 function in the presence of apoptotic cells can accelerate wound healing in the skin.

## Glycogen reserves and aerobic glycolysis fuel enhanced efferocytosis in dendritic cells

To better understand how loss/inhibition of Slc7a11synergizes with apoptotic cells, we performed RNAseq of control and Slc7a11-deficient dendritic cells engulfing apoptotic cells (Fig. 3a). While there was very little basal difference in gene expression between WT and Slc7a11 KO dendritic cells, efferocytic Slc7a11-deficient DCs had 191 differentially expressed genes (125 upregulated and 66 downregulated) compared. These differentially expressed genes were linked to biological processes including metabolism, protein synthesis, mitochondrial and ER function, transcriptional regulation, and wound healing (Fig. 3b, Extended data 5a). Metabolic function was the most represented transcriptional program in Slc7a11-deficient DCs and included genes associated with gluconeogenesis (*Gpt2*, *Dyrk1b*,

*Hlcs*, *Pck2*)[41,42], diabetes and obesity (*Gdf15*, *Pck2*)[43,44] amino acid synthesis (*Asns*, *Phgdh*), glutamate metabolism (*Aldh18a1*, *Psat1*, *Gpt2*, *Got1*), and lipid metabolism (*Cyb5r1*, *Soat2*, *Acaa1b*, *Cd5l*).

In macrophages aerobic glycolysis of glucose is critical for the initial efferocytosis as well as the continued uptake of additional apoptotic corpses[17]. Dendritic cells have a unique feature among phagocytes in that they possess intracellular glycogen reserves[45]; interestingly, genes related to gluconeogenesis (i.e. generation of glucose) were one of the top hits in the RNAseq of Slc7a11-deficient efferocytic dendritic cells. Thus, we considered whether Slc7a11-deficient dendritic cells might have increased capacity to convert some of their glycogen reserves to generate more glucose to fuel aerobic glycolysis and thereby promote increased efferocytosis. We compared glycogen reserves between control and Slc7a11-deficient dendritic cells, as well as WT dendritic cells before and after erastin treatment. Both Slc7a11-deficient BMDC as well as erastin-treated WT cDC1 showed reduced intracellular glycogen (Fig. 3c). Importantly, addition of the glycogen phosphorylase inhibitor CP-91149 reversed glycogen levels in erastin-treated BMDC almost to DMSO control (Fig. 3d). Addition of CP-91149 also strongly abrogated the erastin-dependent increase in efferocytosis (Fig. 3d), supporting the notion that glycogenolysis contributes to greater DC efferocytosis. We took two more approaches to validate a role for glycogenolysis at fueling enhanced efferocytosis in Slc7a11 KO/inhibited dendritic cells. First, siRNA mediated knockdown of *Pygl*, which encodes glycogen phosphorylase involved in glycogen breakdown (Extended data 6a), mitigated the increased efferocytosis after Slc7a11 inhibition in BMDC (Extended data 6b), although *Pygl* gene expression *per se* is unaffected by Slc7a11 inhibition (Extended data 6e-f). Second, another inhibitor of glycogen phosphorylase (DAB) also strongly abrogated increased efferocytosis by Slc7a11-inhibited (Extended data 6c) or Slc7a11-KO dendritic cells (Extended data 6d). Collectively, these data confirm the contribution of glycogen breakdown to boosted DC efferocytosis after Slc7a11 inhibition.

We also assessed another rate-limiting enzyme glycogen synthase (Gys1), which affects the synthesis of glycogen. Surprisingly, erastin treatment increased glycogen synthase (Gys1) protein levels, although the inhibitory phosphorylation of Gys1 on Ser641, Ser645 and Ser649 on GYS1 by GSK3β also concurrently increased after erastin treatment. Thus, while there may be more Gys1 protein after erastin treatment, this might be in an inhibitory state and may not promote glycogen synthesis (Extended data 6 a,e,f). Further, α-glucosidase (Agl), the debranching enzyme involved in glycogen degradation was increased after erastin

235 treatment (Extended data 6 a,e,f). Thus, the depleted glycogen pools in Slc7a11KO/inhibited
236 dendritic cells might comprise alterations in both synthesis and degradation of glycogen.

237 Next, we asked whether aerobic glycolysis was important for dendritic cells
238 efferocytosis. In *Seahorse* analysis, steady-state Slc7a11-deficient or erastin treated dendritic
239 cells showed greater aerobic glycolysis (ECAR) and decreased oxygen consumption rate
240 (OCR, suggestive of mitochondrial oxidative phosphorylation), along with a significantly
241 reduced spare respiratory capacity (Extended data 7a, b). During efferocytosis, both WT and
242 erastin-treated dendritic cells showed greater aerobic glycolysis (ECAR) and less OCR
243 (Extended data 7a). To validate the influence of Slc7a11 inhibition on glycolysis, we
244 performed glycolysis stress test on BMDC either in the presence or absence of apoptotic
245 targets and erastin treatment after glucose starvation. The increased glycolytic rate with
246 Slc7a11 KO BMDC was further augmented with efferocytosis (Fig. 3e middle panel). Of
247 note, the increased glycolysis was comparable between Slc7a11 KO and erastin-treated WT
248 BMDC (Fig. 3e right panel). Although glycolytic rate (ECAR) was increased in WT BMDCs
249 exposed to either apoptotic cells or erastin (Fig. 3e left panel), coupling erastin with apoptotic
250 cells did not further increase ECAR in WT DCs. Collectively, these results suggest that
251 Slc7a11 KO / erastin-treated DCs increase their glycolysis to meet the bioenergetic demands.

252 To test whether aerobic glycolysis plays a role in the enhanced efferocytosis by
253 Slc7a11-deficient dendritic cells, we used several pharmacological inhibitors. First, a non-
254 metabolizable glucose analogue 2-deoxyglucose (2-DG) abrogated the enhanced
255 efferocytosis due to Slc7a11 inhibition (Fig. 3f). Second, 3-BP, a cell-permeable inhibitor of
256 hexokinase-II mediated glycolysis (Fig. 3f), also dampened the erastin effect. When we asked
257 if alternative fuel substrates such as glutamine or pyruvate could be used by Slc7a11-
258 inhibited dendritic cells, this did not appear to be the case (Extended data 7d). Similarly,
259 reducing glutamate levels via glutaminase inhibitor CB-839, did not lead to higher
260 efferocytosis (Extended data 7d). Of note, none of the inhibitors interfered with dendritic cell
261 viability (Extended data 7c). These data suggest that conversion of glycogen stores in
262 dendritic cells to glucose and the subsequent aerobic glycolysis promote enhanced
263 efferocytosis by Slc7a11-deficient dendritic cells. Intriguingly, co-administration of CP-
264 91149 or 3-BP in the erastin regimen reversed the accelerated wound healing *in vivo*
265 (Extended data 8), linking glycolysis/glycogen dynamics with efferocytosis in cutaneous
266 wound healing.

We then performed targeted metabolomic profiling of the cell pellets from dendritic cells lacking Slc7a11, with Slc7a11-inhibition, and controls, both at steady-state and during efferocytosis (Extended data 9). First, Slc7a11 KO and erastin-treated conditions had similar cellular cysteine (~50% reduction) compared to controls, confirming the role of Slc7a11. Second, serine levels were comparable at the steady-state, but significantly increased upon efferocytosis in all conditions (perhaps derived from the ingested corpse). Third, the levels of other amino acids such as lysine, histidine, asparagine and alanine were unaffected in dendritic cells at steady state by knockout or inhibition of Slc7a11; but these amino acids increased (irrespective of the genotype) in efferocytic dendritic cells likely derived from the apoptotic cargo. Further, targeting several genes involved in the synthesis of serine from glucose (*Phgdh*, *Psat1*, *Psph*) and also *Cth*, which promotes the synthesis of cysteine from serine, either by siRNA targeting or by pharmacological inhibition did not alter the efferocytosis of control cells or the enhanced efferocytosis of erastin-treated dendritic cells (not shown). Collectively, these data suggest that serine, which is a precursor for cysteine, or other amino acids, do not appear to contribute to the enhanced efferocytosis in Slc7a11-inhibited dendritic cells.

## Slc7a11 inhibition and rGDF15 facilitate wound healing in diabetic mice

Non-healing chronic wounds are a serious complication impacting the quality of life in diabetic patients[56]. To test the relevance of Slc7a11 in diabetic wound healing, we used leptin receptor-deficient *db/db* mice, which represent a model of human type 2 diabetes with obesity and hyperglycemia. As expected, wound healing is impaired in *db/db* mice in the skin excision model, with a delay of nearly 3 days to reach half-maximal closure (Fig. 4a, and ref [46]). Strikingly, *Slc7a11* expression was 200-fold higher on day 4 in the wounds of *db/db* mice compared to normoglycemic C57BL/6 mice (Fig. 4b). To test whether Slc7a11 inhibition might affect diabetic wound healing, we treated *db/db* mice post-wounding with erastin alone and via the erastin regimen (with apoptotic cell co-administration). Diabetic wounds treated only with erastin displayed acceleration of closure, likely because there are enough uncleared apoptotic cells in the diabetic wounds (Fig. 4c). While wounds of C57BL/6 mice reached ~400 apoptotic cells at day 4 (Fig. 2i) and dropped to 50 at day 13, the diabetic wounds still had ~400 cleaved caspase $3^+$ cells at day 13 (Fig. 4c) reflecting the increased apoptotic load. The erastin regimen improved healing in the *db/db* mice as early as day 2 after wounding, continuing through full closure by day 13, and reaching 50% closure of initial wound 2-3 days earlier than untreated *db/db* mice (Fig. 4d).

Next, we tested the link between efferocytosis and the accelerated wound closure in the *db/db* mice. In *ex vivo* analysis, dendritic cells from *db/db* mice showed reduced efferocytosis, with the difference more pronounced at earlier time points (Fig. 4e) (analogous to macrophages from diabetic mice[13]). Strikingly, erastin 'rescued' the defective efferocytosis of diabetic *db/db* dendritic cells (Fig. 4e). Consistent with this *ex vivo* phenotype, the erastin regimen substantially reduced uncleared apoptotic cells in the wounds of *db/db* mice (Fig. 4f). While erastin reduces the apoptotic cell burden with or without an apoptotic cell bolus in the *db/db* mice, the apoptotic cell burden in the control C57BL/6 mice was only reduced in the erastin regimen. Although there is overall less apoptotic cell burden in the wounds of control mice compared to diabetic mice, the addition of apoptotic bolus promotes the effect of erastin (Extended data 10a, b).

As the combination of Slc7a11 inhibition together with apoptotic cell addition to the wounds provided the most efficient wound healing, and efferocytic phagocytes also secrete factors that are known to provide beneficial effects in tissues[47], we asked whether secreted factors from efferocytic Slc7a11-deficient dendritic cells may contribute to the accelerated healing. We purified supernatants from efferocytic wild type and Slc7a11 KO dendritic cells and added these exogenous supernatants to the excision wounds. Mice treated with efferocytic supernatants from efferocytic Slc7a11-deficient dendritic cells exhibited faster wound closure compared to WT dendritic cells (Fig. 4g).

Soluble factors, including members of TGF-β superfamily (TGF-β 1-3) are released by efferocytic phagocytes, and can affect wound healing[48]. Mining the transcriptome of efferocytic Slc7a11-deficient dendritic cells, we noted upregulation of *Gdf15* which encodes growth differentiation factor 15 (Fig. 4h). GDF15, a member of the TGF-β superfamily, has been associated with obesity, diabetes, cancer, cardiovascular, kidney disorders, and tissue regeneration[43,49,50]. GDF15 protein was significantly increased in the supernatants of efferocytic dendritic cells from Slc7a11-deficient mice compared to that of wild-type littermates (Fig. 4h). GDF15 levels increased (2-5 fold) at day 2 post excisional skin wounding compared to unwounded skin and remained high even at later stages of healing (day 8) (Fig. 4i). When we tested GDF15-deficient mice in the excisional skin biopsy model, they displayed larger wounds at day 2 compared to littermate control mice (Fig. 4j), and this correlated with greater *Slc7a11* expression in the wounds (Fig.4b). Consistent with the notion that GDF15 is produced downstream of efferocytosis, GDF15-deficient dendritic cells showed similar *Slc7a11* expression at the steady-state (Extended data 10c) and comparable

efferocytosis as controls (Extended data 10d). When we treated GDF15 KO mice with erastin, we detected a partial enhancement in wound-closure compared to vehicle (Extended data 10e), implying both GDF15-dependent and GDF15-independent effects of Slc7a11 blockade in wound healing.

Interestingly, the levels of GDF15 are almost undetectable in the wounds of *db/db* mice compared to normoglycemic (B6) mice (Fig. 4i). Therefore, when we asked whether recombinant GDF15 (rGDF15) might help wound healing in *db/db* mice, application of rGDF15 significantly improved wound healing (Fig. 4k). Thus, reduced efferocytosis and lower GDF15 levels, both of which correlate with high Slc7a11 expression in the diabetic-prone mice contribute to the delayed skin wound healing. Thus, Slc7a11 inhibition at the wound site can improve diabetic wound healing via at least two modalities: improving cell clearance and via factors such as GDF15 from the efferocytic cells that promote wound healing.

## Discussion

These data via a combination of *in vitro*, *ex vivo*, *in vivo* approaches, and metabolomics, advance new concepts on dendritic cell-mediated efferocytosis and tissue regeneration/wound healing. First, expression of multiple membrane proteins and transporters are modulated during apoptotic cell engulfment by dendritic cells, among which the amino acid transporter Slc7a11acts as a negative regulator of efferocytosis. It is unclear why this negative regulator of efferocytosis would be upregulated following wounding, although concurrent upregulation of negative and positive regulators (i.e. the simultaneous pressing of the 'accelerator' and the 'brake') is likely part of a finely-balanced signaling regulation *in vivo,* as has been seen in T cells during antigen receptor signaling, in fibroblasts during growth factor stimulation, and in macrophages during FcR-mediated phagocytosis. Mechanistically, the enhanced efferocytosis in Slc7a11-deficient dendritic cells is fueled in part by greater aerobic glycolysis, where the source of glucose is derived from glycogen stores, a feature somewhat unique to dendritic cells among phagocytes. This work also reveals dendritic cells as relevant players in clearing apoptotic cells during cutaneous skin injury. Most strikingly, the combination of Slc7a11 blockade together with apoptotic cells improve the wound healing kinetics. This accelerated wound healing is not only seen in wild type mice, but in diabetic-prone *db/db* mice. Transcriptomics of Slc7a11-deficient dendritic cells identified GDF15 as one key extracellular mediator released from efferocytic dendritic

cells that facilitates wound closure downstream of Slc7a11. Collectively, this work, starting from the unbiased transcriptomics of efferocytic dendritic cells to identifying Slc7a11 as a brake on dendritic cell phagocytosis and mechanistic studies, reveals a new approach to improve cutaneous wound healing. This strategy could be relevant for diabetic wound management and other skin conditions associated with chronic inflammation.

## Methods

**Murine tissue processing.** Cells from ears of Slc7a11 KO and control littermates were isolated as previously described[51]. Briefly, ear skin samples were collected by cutting at the ear base and were incubated overnight at 4°C with 200 μg/ml Dispase II (from Bacillus polymerase grade 2; Roche, Basel, Switzerland) to facilitate manual cutting and isolation of cells. Small skin pieces were further digested with 1.5 mg/ml collagenase type 4 (Worthington, Lakewood, NJ) and 10 U DNase (Roche) in RPMI medium buffered with HEPES and supplemented with 2% fetal calf serum. The suspension was resuspended every 30 minutes and provided with fresh digestion buffer for a total of 90 minutes at 37°C. After digestion, the cell suspension was filtered to remove debris and clots. For spleen single-cell suspensions, spleens were digested in RPMI medium supplemented with 0.01 U/ml DNase I (Roche) and 0.02 mg/ml Liberase (Roche) for 30 min. Red blood cells were removed with 1x solution of RBC lysis buffer (Biolegend; #420301). For bone-marrow progenitors, bone marrow was isolated from femurs and tibia of 8- to 12-week-old mice.

**Cell isolation.** Single-cell suspensions of digested ears and spleens were further enriched for phagocytes by depleting lymphocyte populations. Depletion was performed using monoclonal biotin-linked antibodies against CD3e (145-2C11, #13-0031-82 eBioscience™), CD19 (eBio1D3-1D3, #13-0193-82 eBioscience™), NK1.1 (PK136, # 13-5941-82 eBioscience™) followed by collection of non-depleted cells using MagniSort™ Streptavidin Negative Selection Beads (#MSNB-6002-74 ThermoFisher). Bone-marrow-derived dendritic cells and macrophages were generated from mice by culturing bone marrow progenitors for 10 days in GM-CSF-supplemented medium and for 6 days in M-CSF-supplemented medium respectively and as previously described[52].

**Flow cytometry and cell sorting.** Immunophenotyping of mouse skin or spleen was performed on single-cell suspensions. Cells were stained with the following anti-mouse, monoclonal, fluorochrome-linked antibodies: CD24-AF488 or -eFluor450 (1: 100; M1/69; #101816 or #48-0242-82, BioLegend), CD11b-BV605 (1: 200; M1/70; #563015, BD Biosciences), CD26-FITC or -BV650 (1: 200; H194-112; #559652 or #740474, BioLegend) , CD11c-BV711 (1: 200; HL3; #563048, BD Biosciences), F4/80-BV785 (1: 200; BM8; #123141, BioLegend), CD45-AF700 (1: 500; 30-F11; # 56-0451-82, ThermoFisher), MHCII (I-A/I-E)-eFluor780 (1: 400; M5/114.15.2; #47-5321-82, ThermoFisher), CD172a (SIRP alpha)- PerCP-eFluor710 (1: 200; P84; #46-1721-82, ThermoFisher), CD103-BUV395 (1: 200; M290; #740238, BD Biosciences), CD64-BV421 or - PE/Cy7 (1: 100; X54-5/7.1;

#139309 or #139314, BioLegend), XCR1-BV650 (1: 200; ZET; #148220, BioLegend) and Fc receptor-blocking antibody CD16/CD32 (1: 300; clone 2.4G2, #553142, BD Biosciences). Viable cells were discriminated using Fixable Viability Dye eFluor 506 (#65-0866-18, ThermoFisher). Prior to measuring, counting beads (#01-1234-42, ThermoFisher) were added to the cells for some experiments. Measurements were performed on a BD LSR Fortessa cytometer and analyzed using FlowJo10 software (Tree Star). Cell sorting was performed on FACS ARIAII and III (BD Biosciences).

**Ferroptosis characterization.** To assess ferroptosis, we utilized BODIPY$^{TM}$ 581/591 (C11-BODIPY) and dihydrorhodamine 123 (DHR123) probes that change their fluorescence properties upon oxidation, as previously described[53]. Briefly, dendritic cells were treated with 5μM erastin (#S7242, Bio-Connect B.V.) or 1μM ML-162 (#AOB1514) or DMSO control prior to addition of fluorescent probes one hour before measurement: 0.5μM C11-BODIPY (#D3861, ThermoFisher) or 1 μM DHR-123 (#85100, Chemical, MI, USA) and 0.5 μM of DRAQ7 cell death stain (#DR70250, BioStatus, Shepshed, UK).

**Determination of glycogen concentration.** The glycogen concentration was measured using a Glycogen Colorimetric/Fluorometric Assay Kit (#GENT-K646-10, BioVision) according to the manufacturer's instructions.

**Determination of glutathione levels.** Glutathione was quantified in dendritic cells two hours after erastin treatment using the GSH/GSSG-Glo Assay luminescence-based system according to the manufacturer's instructions (#V6611, Promega). GSH/GSSG ratios are calculated from luminescence measurements (in relative light units, RLU) and after interpolation of glutathione concentrations from standard curves. Data for both glycogen and glutathione are reported as fold change from DMSO (vehicle)-treated cells or from WT cells.

**Seahorse analysis.** 100000 BMDC were seeded on a *Seahorse* 96-well tissue culture plate (Agilent Technologies). The plate was allowed to stand for 30mins for the cells to settle before placing it in the incubator overnight. The adhered cells were treated with 5μM erastin (#S7242, Bio-Connect B.V) or 200μM CP-91149 (#S2717, Bio-Connect B.V.) 2 hours prior to Seahorse analysis. The cells were switched to serum-free Seahorse media before the assay according to the manufacturer's instructions. For basal ECAR and OCR, the cells were subjected to XF Real Time ATP Rate kit (#103592-100, Agilent Technologies). For assessment of respiratory capacity, cells were subjected to XF Cell Mito Stress Test Kit (#103015-100, Agilent Technologies). The sequential injection of Oligomycin, FCCP, and rotenone/Antimycin A were done at 1.5μM, 1.0μM and 0.5μM respectively. For cells

subjected to Seahorse XF Glycolysis Stress Test Kit (#103020-100, Agilent Technologies), the sequential injection of glucose, oligomycin, and 2-DG were done at 10mM, 1mM and 50mM respectively. At the beginning of the assay, the medium was changed to unbuffered, glucose-free DMEM (Sigma-Aldrich Cat# D5030, pH 7.35 at 37 °C) supplemented with 2mM glutamine.

**Efferocytosis assays.** For induction of apoptosis, human Jurkat T cells were with stained with CypHer5E (#PA15401, GE Healthcare) or TAMRA (#C-1171, Invitrogen) or pHrodo™ Green STP Ester (# P35369, ThermoFisher), resuspended in RPMI with 5% fetal calf serum, treated with 150 mJ/cm$^2$ ultraviolet C irradiation (Stratalinker) and incubated for 4 h at 37 °C with 5% $CO_2$. Dendritic cells were incubated with apoptotic targets at a 1:5 phagocyte:target ratio for the indicated times. Phagocytosis was assessed by a flow cytometry-based assay[21] or by Incucyte Live-cell imaging. As alternative targets for phagocytosis, dendritic cells were incubated with pHrodo™ Green E. *coli* BioParticles™ (#P35366, ThermoFisher) or Streptavidin Fluoresbrite® YG Microspheres, 2.0µm (for simplicity, beads) at a 1:5 phagocyte:target ratio for the indicated times. When applicable, cells were pretreated for 1 hour with 5µM erastin (#S7242, Bio-Connect B.V), 200µM CP-91149 (#S2717, Bio-Connect B.V.), 0.2mM 2-DG (2-Deoxy-D-glucose; #D8375-1G, Sigma), 5µM UK5099 (#PZ0160, Sigma), 40µM DON (6-Diazo-5-oxo-L-norleucine; #D2141-5MG, Sigma), 10µM 3-BP (3-Bromo-2-oxopropionic acid, #376817-M, Sigma), 10mM Glutamate (#6106-04-3, Sigma), 0.5µM Ferrostatin-1(S7243, Bio-Connect B.V.), 1µM FCCP (#HY-100410, Bio-Connect B.V.), 100µM MitoTEMPO (#SML0737, Sigma), 1-2µM L-Glutathione Reduced (#G4251-10G, Sigma), 50µM L-Buthionine-(S,R)-sulfoximine) or BSO (#S9728, Bio-Connect B.V.), 1mM 1,4-Dideoxy-1,4-imino-D-arabinitol hydrochloride or DAB (#20939-5, Cayman Chemical), 2µM CB-839 (#S7655, Bio-Connect B.V.) before addition of targets.

**siRNA experiments.** Dendritic cells were treated with SMARTpool: Accell Slc7a11 siRNA (#E-047420-00-0010), Accell Slc7a1 siRNA (#E-042922-00-0005), Accell Slc7a5 siRNA (#E-041166-00-0010), Accell Pygl siRNA(#E-046873-00-0005) or Accell Non-targeting siRNA #1 (#D-001910-01-05) and Accell Non-targeting siRNA #4 (# D-001910-04-05) from Dharmacon, according to the manufacturer's instructions, 2 days before the engulfment assay.

**qRT-PCR.** Total RNA was extracted from cells using the RNeasy Mini Kit (Qiagen) and cDNA was synthesized using Sensifast cDNA Synthesis Kit (#BIO-650504), according to the manufacturer's instructions. Quantitative gene expression analysis for mouse genes was performed using mouse-sequence specific Taqman probes that are non-cross reactive with human sequences (Applied Biosystems), run on a Roche Lightcycler 480 -384.

**ELISA.** GDF15 levels were measured in supernatants of dendritic cells or total skin lysates by using Mouse/Rat GDF-15 Quantikine ELISA Kit (#MGD150, R&D Systems). For skin lysates, total (shaved skin) was lysed in 50mM Tris–HCl (pH 8,5) using the Precellys 24 tissue homogenizer and 25μg lysate per sample were used for ELISA.

**RNA sequencing.** Wild type or Slc7a11-deficient BMDC were co-cultured with apoptotic Jurkat cells for 4 h, unbound Jurkat cells were removed by washing with PBS and engulfing BMDC were isolated by sorting with BD FACSAria$^{TM}$III Cell Sorter. Total RNA was extracted, and an mRNA library was prepared using the IlluminaNovoseq6000platform by Novogene. HISAT2 was selected to map the filtered sequenced reads to the reference genome. BAM files containing mapping results were counted using the feature Counts function in the R package Rsubread. Counting was performed using both mouse and human genomes for comparison although downstream analyses were only performed on mouse data. DEG analysis was then performed using DESeq2 considering all genes with FDR $\leq 0.05$ and $0.58 \leq \text{Log2FC} \leq -0.58$. All genes that resulted from the analysis were curated using multiple methods, including literature mining and function determination (known or predicted) via UniProt.

**scRNA sequencing and analysis.** Single-cell RNA-sequencing (scRNAseq) datasets on live cells sorted from control wild-type (WT: Cre-negative OTULIN$^{fl/fl}$; n=1) skin and lesional (L; n=3) and non-lesional (NL; n=2) $\Delta^{Ker}$OTULIN skin are fully described in Hoste *et al.*[54]

**Bioinformatics analysis.** Gene sets were tested for unidirectional enrichment and visualized using the Triwise package. Proximity represents upregulation in more than one population, and the distance from the origin represents the strength of expression. Gene expression data sets analyzed in RStudio Version 1.2.1335 and based on mean values of the normalized gene counts of each of three dendritic cell (DC) populations (lung, skin and spleen) extracted from ImmGen Microarray V1 data set "GSE15907".

**Targeted metabolomics.** Metabolite extracts have been analyzed by either reverse phase chromatography or hydrophilic interaction chromatography (HILIC). For reverse phase

chromatography, metabolite extracts have been dried down and resolved in an equal volume of 0.1% formic acid in water. 1 ul of this extract has been separated on a Kinetex (Phenomenex) C18 column (100 Å, 150 x 2.1 mm) connected with the respective guard column, employing a 7-minute-long linear gradient from 99% A (1 % acetonitrile, 0.1 % formic acid in water) to 60% B (0.1 % formic acid in acetonitrile) at a flow rate of 80 µl/min. UV detection has been user for quality control only. Detection and quantification has been done by on-line tandem mass spectrometry (LC-MS/MS), employing the selected reaction monitoring (SRM) mode of a TSQ Altis mass spectrometer (Thermo Fisher Scientific), using the following transitions in the positive ion mode: 147 *m/z* to 84 *m/z* (lysine), 156 *m/z* to 110 *m/z* (histidine), 175 *m/z* to 70 *m/z* (arginine), 223 *m/z* to 88 *m/z* (cystathionine), 241 *m/z* to 74 *m/z* (cystine), 399 *m/z* to 250 *m/z* (SAM), 76 *m/z* to 30 *m/z* (glycine), 106 *m/z* to 60 *m/z* (serine), 133 *m/z* to 74 *m/z* (asparagine), 134 *m/z* to 74 *m/z* (aspartic acid), 147 *m/z* to 130 *m/z* (glutamine), 148 *m/z* to 84 *m/z* (glutamic acid), 90 *m/z* to 44 *m/z* (alanine), 120 *m/z* to 74 *m/z* (threonine), 122 *m/z* to 76 *m/z* (cysteine), 116 *m/z* to 70 *m/z* (proline), 118 *m/z* to 72 *m/z* (valine), 150 *m/z* to 133 *m/z* (methionine), 132 *m/z* to 86 *m/z* (leucine and isoleucine), 182 *m/z* to 36 *m/z* (tyrosine), 385 *m/z* to 136 *m/z* (S-adenosyl-homocysteine), 166 *m/z* to 133 *m/z* (phenylalanine), 298 *m/z* to 136 *m/z* (MTA), 205 *m/z* to 188 *m/z* (tryptophan). In an independent analysis, 1 µl of the original sample was injected onto a polymeric iHILIC-(P) Classic HPLC column (HILICON, 100 x 2.1 mm; 5 µm) and the respective guard column, operated at a flow rate of 100 µl/min. The HPLC (Ultimate 3000 HPLC system; Dionex, Thermo Fisher Scientific) was directly coupled via electrospray ionization to a TSQ Quantiva mass spectrometer (Thermo Fisher Scientific). A linear gradient (A: 95% acetonitrile 5%, 10 mM aqueous ammonium acetate; B: 5 mM aqueous ammonium bicarbonate) starting with 15% B and ramping up to 60% B in 9 minutes was used for separation. The following SRM transitions were used for quantitation ion the negative ion mode: 87 *m/z* to 43 *m/z* (pyruvate), 89 *m/z* to 43 *m/z* (lactate), , 808 *m/z* to 408 *m/z* (acetyl-CoA), 766 *m/z* to 408 *m/z* (CoA), 117 *m/z* to 73 *m/z* (succinate), 145 *m/z* to 101 *m/z* (α-ketoglutarate), 169 *m/z* to 97 *m/z* (dihydroxyacetone phosphate), 115 *m/z* to 71 *m/z* (fumarate), 133 *m/z* to 71 *m/z* (malate), 229 *m/z* to 97 *m/z* (pentose phosphates), 124 *m/z* to 80 *m/z* (taurine), 259 *m/z* to 97 *m/z* (hexose phosphates), 259 *m/z* to 97 *m/z* (hexose phosphates), 191 *m/z* to 111 *m/z* (citrate). Data interpretation was performed using TraceFinder (Thermo Fisher Scientific). Authentic metabolite standards were used for determining collision energies and retention times and for validating experimental retention times by standard addition.

**Mice.** The following mouse lines were used: C57BL/6J, Slc7a11KO[55] and littermate wild-type, B6.BKS(D)-Leprdb/J (*db/db*) and PDGFRα-H2B-eGFP reporter mice[56]. For the GDF15KO mice, the ES cells (as in ref [57]) were obtained from EUCOMM and newly generated in our transgenic mouse core facility. Mice were housed in individually-ventilated cages at the VIB Center for Inflammation Research, in a specific pathogen-free animal facility. Mice were housed under 14:10 (light:dark) light cycles, at 21 degrees (C), and 60% humidity. These conditions are checked and maintained by vivarium staff daily. All experiments on mice were conducted according to institutional, national and European animal regulations. Animal protocols were approved by the ethics committee of Ghent University (EC file #2020-049).

**Skin wounding and erastin regimen.** Full-thickness wounds were made as previously described[56,58]. Briefly, wounds were made on shaved back skin by using 8-mm punch biopsy needles (Stiefel Instruments) under analgesia and general anesthesia in 8-week-old female C57BL/6J, B6.BKS(D)-Leprdb/J (db/db), GDF15KO, Slc7a11KO and control littermates. For wound healing experiments, assuming standard deviations of 10– 15%, an experimental group of $n$ = 10 is needed to obtain statistical power of 90% (significance level 0.05) and detect a difference between means of 20%, using two-tailed paired T-testing. No animals were excluded from any experiment.

For topical applications, mice were intradermally injected with Imidazole ketone erastin (IKE at 20 mg $kg^{-1}$ in 100 µl PBS; MedChemExpress, #HY-114481) or recombinant human GDF-15 (0.7 mg $kg^{-1}$ in 100 µl PBS; R&D Systems, #9279-GD-050) or RSL3 (20 mg $kg^{-1}$ in 100 µl PBS; Sellechem, #S8155) or the respective vehicle controls (DMSO or 4 mM HCl in 100 µl PBS) at the time of wounding and for two consecutive days. For the experiments indicated as 'erastin regimen' or vehicle regimen, 5 million apoptotic Jurkat cells were administrated once on day 0 in 50 µl PBS on top of back skin immediately after full-thickness excision biopsy. When indicated, the compounds CP-91149 (50 mg $kg^{-1}$) and 3-BP (50 mg $kg^{-1}$) were topically administrated on the wounds, on day 0 to day 2. For the mice injected intradermally with supernatants from efferocytic dendritic cells, supernatants from dendritic cells cultured with apoptotic Jurkat cells for 16h were collected, centrifuged to eliminate debris and frozen or lyophilized for preservation.

**Histology and Immunohistochemistry.** Skin biopsies were fixed using 4% paraformaldehyde overnight. Following dehydration steps, samples were embedded in paraffin and sectioned at 10 µm thickness. Dewaxed paraffin skin sections were stained with

Hematoxylin and Eosin stains or subjected to heat-mediated antigen retrieval (citrate buffer; pH=6), and apoptotic cells were evaluated with cleaved caspase-3 antibody (1: 100; Cell Signaling Technology #9664). Slides were incubated with secondary antibody followed and peroxidase activity was detected with diaminobenzidine (DAB)-substrate kit (Cell signaling, #8059P). Nuclei were counterstained with Hematoxylin staining. Cleaved caspase-$3^+$ positive cells were manually counted by using Zen software by Zeiss. Quantification of cleaved caspase-$3^+$ was cells was done by an independent researcher, who was blinded to the genotypes or treatment.

**Immunofluorescence.** Dewaxed paraffin skin sections were subjected to heat-mediated antigen retrieval (citrate buffer; pH=6), blocked with 0.5% fish skin gelatin, 4% BSA in PBS and labelled with biotin anti-CD11c Ab (1:200, BD Pharmingen #553800), anti-Slc7a11 Ab (1:200, in-house developed[59]) or cleaved caspase-3 antibody (1:100; Cell Signaling Technology #9664). As secondary antibodies streptavidin 594 AlexaFluor (1:2000) and donkey-anti-rabbit DyLight 488 (1:2000; Abcam ab#96919) were used in combination with DAPI. For immunofluorescence analysis of frozen tissue, mouse back skin was embedded in OCT and tissue blocks were sectioned (10 mm) with a cryostat and mounted on SuperFrost Plus slides (ThermoFisher). After sectioning, tissue was fixed in 4% paraformaldehyde for 1h. After fixation, tissue was washed with PBS and was blocked in buffer containing 5% normal goat serum, 1% bovine serum albumin, 1% fish gelatin, 0.3% Triton X-100 in PBS, for 2 hrs at room temperature before incubation in primary antibodies (1:500 Itgα5, clone 5H10-27, #AB_394779; BD Biosciences or Ki67, clone SolA15, #AB_10854564; ThermoFisher), at 4C overnight. Samples were washed three times with PBS prior to incubation with secondary antibodies for 2hr at room temperature.

**Immunoblotting.** BMDC were seeded in 6-well-plates at a concentration of 500,000 cells per well. After 12h of treatment with 5μM erastin (#S7242, Bio-Connect B.V) or DMSO control, cells were collected and lysed directly in sample buffer. After protein denaturation, SDS–PAGE was performed using 10% gradient Bis-Tris gels. Primary antibodies were used for overnight incubation, followed by 1-h incubation with secondary antibody and chemiluminescence detection. Antibodies were used at the following dilutions: 1:1,000 (Anti-phospho-GlycogenSynthase (Ser641/Ser645) #07-817; Sigma, anti-GYS1 Monoclonal Antibody (J.18.5), #MA5-15022; ThermoFisher, anti-PYGL Polyclonal antibody #15851-1-AP; Proteintech, anti-AGL/Alpha-glucosidase antibody [EPR8880], #ab133720; Abcam); 1:5,000 (Anti-beta Actin antibody - Loading Control HRP; mAbcam #8226).

**Statistical analysis.** Statistical significance was determined using GraphPad Prism 9, using unpaired Student's two-tailed *t*-test, one-way ANOVA or two-way ANOVA. *$P$<0.05, **$P$<0.01, ***$P$ < 0.001, ****$P$ < 0.0001 were considered significant.

**Acknowledgements.** We thank members of the Ravichandran laboratory and Bartosz Wiernicki for discussions and input, Tania Løve Aaes for Tri-wise analysis, and the VIB-Transgenic Core, VIB-Flow Cytometry Core, VIB-Bioimaging Core, and VIB-Nucleomics Core. We also thank the VBCF Metabolomics Facility, Vienna, for metabolomics analysis. K.S.R. is supported by FWO (Odysseus grant G0F5716N, EOS DECODE 30837538), Special Research Fund UGent (iBOF BOF20/IBF/037), European Research Council (ERC) (grant agreement no. 835243), grants from NHLBI (P01HL120840), NIAID (R01AI159551), NIGMS (R35GM122542), and the Center for Cell Clearance/University of Virginia School of Medicine; and G.V.L. is supported by Foundation against Cancer (STK 2014-142 and STK 2018-093) and FWO (G020216N). S.M. is supported by postdoctoral *Marie Skłodowska-Curie Actions* individual fellowship (800446) from the European Commission, Horizon 2020 Research and Innovation Framework Program, and E.H. is supported by an FWO postdoctoral fellowship and FWO research grant. Additional support was received through the FWO Postdoctoral Fellowship (1227220N to P.M.). Mouse images and elements were created with BioRender.com with a purchased license or from public databases that allow their reuse.

**Author contributions.** S.M. and K.S.R. designed all experiments and wrote the manuscript. S.M. performed most experiments. E.H. provided conceptual advice and help for skin wound healing experiments. P.M. helped design and assisted with the metabolism-related experiments, B.N.K assisted with histology studies, and H.K.L.D. assisted with immunoblotting experiments. J.P. assisted with bioinformatic analysis. K.L, R.V.D.C, P.J., G.V.L., D.E., A.M., provided mice, technical advice, and input on the manuscript.

## Ethics declarations

All animal procedures associated with this work were conducted after approval by the institutional ethical committees.

## Competing interests

The authors declare no competing interests.

## Data availability statement

All of the sequencing data associated with this work have been deposited in public data bases. Any other related information is available upon request.

Address correspondence to: kodi@wustl.edu or sophia.maschalidi@irc.vib-ugent.be

## References


1 Henson, P. M. Cell Removal: Efferocytosis. *Annu Rev Cell Dev Biol* **33**, 127-144, doi:10.1146/annurev-cellbio-111315-125315 (2017).

2 Boada-Romero, E., Martinez, J., Heckmann, B. L. & Green, D. R. The clearance of dead cells by efferocytosis. *Nat Rev Mol Cell Biol* **21**, 398-414, doi:10.1038/s41580-020-0232-1 (2020).

3 Morioka, S., Maueroder, C. & Ravichandran, K. S. Living on the Edge: Efferocytosis at the Interface of Homeostasis and Pathology. *Immunity* **50**, 1149-1162, doi:10.1016/j.immuni.2019.04.018 (2019).

4 Cabeza-Cabrerizo, M., Cardoso, A., Minutti, C. M., Pereira da Costa, M. & Reis, E. S. C. Dendritic Cells Revisited. *Annu Rev Immunol* **39**, 131-166, doi:10.1146/annurev-immunol-061020-053707 (2021).

5 Guermonprez, P. & Amigorena, S. Pathways for antigen cross presentation. *Springer Semin Immunopathol* **26**, 257-271, doi:10.1007/s00281-004-0176-0 (2005).

6 Albert, M. L., Sauter, B. & Bhardwaj, N. Dendritic cells acquire antigen from apoptotic cells and induce class I-restricted CTLs. *Nature* **392**, 86-89, doi:10.1038/32183 (1998).

7 Gallucci, S., Lolkema, M. & Matzinger, P. Natural adjuvants: endogenous activators of dendritic cells. *Nat Med* **5**, 1249-1255, doi:10.1038/15200 (1999).

8 Blander, J. M. & Medzhitov, R. On regulation of phagosome maturation and antigen presentation. *Nat Immunol* **7**, 1029-1035, doi:10.1038/ni1006-1029 (2006).

9 Khanna, S. *et al.* Macrophage dysfunction impairs resolution of inflammation in the wounds of diabetic mice. *PLoS One* **5**, e9539, doi:10.1371/journal.pone.0009539 (2010).

10 Wetzler, C., Kampfer, H., Stallmeyer, B., Pfeilschifter, J. & Frank, S. Large and sustained induction of chemokines during impaired wound healing in the genetically diabetic mouse: prolonged persistence of neutrophils and macrophages during the late phase of repair. *J Invest Dermatol* **115**, 245-253, doi:10.1046/j.1523-1747.2000.00029.x (2000).

11 Moulik, P. K., Mtonga, R. & Gill, G. V. Amputation and mortality in new-onset diabetic foot ulcers stratified by etiology. *Diabetes Care* **26**, 491-494, doi:10.2337/diacare.26.2.491 (2003).

12 Lenz, A., Heine, M., Schuler, G. & Romani, N. Human and murine dermis contain dendritic cells. Isolation by means of a novel method and phenotypical and functional characterization. *J Clin Invest* **92**, 2587-2596, doi:10.1172/JCI116873 (1993).

13 Seneschal, J., Clark, R. A., Gehad, A., Baecher-Allan, C. M. & Kupper, T. S. Human epidermal Langerhans cells maintain immune homeostasis in skin by activating skin resident regulatory T cells. *Immunity* **36**, 873-884, doi:10.1016/j.immuni.2012.03.018 (2012).

14 Mirza, R., DiPietro, L. A. & Koh, T. J. Selective and specific macrophage ablation is detrimental to wound healing in mice. *Am J Pathol* **175**, 2454-2462, doi:10.2353/ajpath.2009.090248 (2009).

15 Shook, B., Xiao, E., Kumamoto, Y., Iwasaki, A. & Horsley, V. CD301b+ Macrophages Are Essential for Effective Skin Wound Healing. *J Invest Dermatol* **136**, 1885-1891, doi:10.1016/j.jid.2016.05.107 (2016).

16 Phillipson, M. & Kubes, P. The Healing Power of Neutrophils. *Trends Immunol* **40**, 635-647, doi:10.1016/j.it.2019.05.001 (2019).

17 Morioka, S. *et al.* Efferocytosis induces a novel SLC program to promote glucose uptake and lactate release. *Nature* **563**, 714-718, doi:10.1038/s41586-018-0735-5 (2018).

18 Kelly, B. & Pearce, E. L. Amino Assets: How Amino Acids Support Immunity. *Cell Metab* **32**, 154-175, doi:10.1016/j.cmet.2020.06.010 (2020).

19 Procaccini, C. *et al.* Signals of pseudo-starvation unveil the amino acid transporter SLC7A11 as key determinant in the control of Treg cell proliferative potential. *Immunity*, doi:10.1016/j.immuni.2021.04.014 (2021).

20 D'Angelo, J. A. *et al.* The cystine/glutamate antiporter regulates dendritic cell differentiation and antigen presentation. *J Immunol* **185**, 3217-3226, doi:10.4049/jimmunol.1001199 (2010).

21 Fotiadis, D., Kanai, Y. & Palacin, M. The SLC3 and SLC7 families of amino acid transporters. *Mol Aspects Med* **34**, 139-158, doi:10.1016/j.mam.2012.10.007 (2013).

22 Merckx, E. *et al.* Absence of system xc(-) on immune cells invading the central nervous system alleviates experimental autoimmune encephalitis. *J Neuroinflammation* **14**, 9, doi:10.1186/s12974-016-0787-0 (2017).

23 Massie, A. *et al.* Time-dependent changes in striatal xCT protein expression in hemi-Parkinson rats. *Neuroreport* **19**, 1589-1592, doi:10.1097/WNR.0b013e328312181c (2008).

24 Mesci, P. *et al.* System xC- is a mediator of microglial function and its deletion slows symptoms in amyotrophic lateral sclerosis mice. *Brain* **138**, 53-68, doi:10.1093/brain/awu312 (2015).

25 Lin, C. H. *et al.* Decreased mRNA expression for the two subunits of system xc(-), SLC3A2 and SLC7A11, in WBC in patients with schizophrenia: Evidence in support of the hypo-glutamatergic hypothesis of schizophrenia. *J Psychiatr Res* **72**, 58-63, doi:10.1016/j.jpsychires.2015.10.007 (2016).

26 Massie, A. *et al.* Dopaminergic neurons of system x(c)(-)-deficient mice are highly protected against 6-hydroxydopamine-induced toxicity. *FASEB J* **25**, 1359-1369, doi:10.1096/fj.10-177212 (2011).

27 Kaleeba, J. A. & Berger, E. A. Kaposi's sarcoma-associated herpesvirus fusion-entry receptor: cystine transporter xCT. *Science* **311**, 1921-1924, doi:10.1126/science.1120878 (2006).

28 Kandasamy, R. K. *et al.* A time-resolved molecular map of the macrophage response to VSV infection. *NPJ Syst Biol Appl* **2**, 16027, doi:10.1038/npjsba.2016.27 (2016).

29 Rabinowitz, J. *et al.* xCT/SLC7A11 antiporter function inhibits HIV-1 infection. *Virology* **556**, 149-160, doi:10.1016/j.virol.2021.01.008 (2021).

30 Robert, S. M. *et al.* SLC7A11 expression is associated with seizures and predicts poor survival in patients with malignant glioma. *Sci Transl Med* **7**, 289ra286, doi:10.1126/scitranslmed.aaa8103 (2015).

31 Koppula, P., Zhuang, L. & Gan, B. Cystine transporter SLC7A11/xCT in cancer: ferroptosis, nutrient dependency, and cancer therapy. *Protein Cell*, doi:10.1007/s13238-020-00789-5 (2020).

32 Hassannia, B., Vandenabeele, P. & Vanden Berghe, T. Targeting Ferroptosis to Iron Out Cancer. *Cancer Cell* **35**, 830-849, doi:10.1016/j.ccell.2019.04.002 (2019).

33 Conrad, M. & Pratt, D. A. The chemical basis of ferroptosis. *Nat Chem Biol* **15**, 1137-1147, doi:10.1038/s41589-019-0408-1 (2019).

34 Jiang, X., Stockwell, B. R. & Conrad, M. Ferroptosis: mechanisms, biology and role in disease. *Nat Rev Mol Cell Biol* **22**, 266-282, doi:10.1038/s41580-020-00324-8 (2021).

35 Zilka, O., Shah, R., Li, B., Friedmann Angeli,, Griesser, M., Conrad, M. & Pratt, D. A. On the Mechanism of Cytoprotection by Ferrostatin-1 and Liproxstatin-1 and the Role of Lipid Peroxidation in Ferroptotic Cell Death. *ACS Cent Sci*, **3**, 232-243, doi: 10.1021/acscentsci.7b00028 (2017).

36 Sato, M., Kusumi, R., Hamashima, S., Kobayashi, S., Sasaki, S., Komiyama, Y., Izumikawa, T., Conrad, M., Bannai, S. & Sato, H. The ferroptosis inducer erastin irreversibly inhibits system xc- and synergizes with cisplatin to increase cisplatin's cytotoxicity in cancer cells. *Sci Rep* **8**, 968, doi:10.1038/s41598-018-19213-4 (2018).

37 Rajesh, A. *et al.* Depletion of langerin(+) cells enhances cutaneous wound healing. *Immunology* **160**, 366-381, doi:10.1111/imm.13202 (2020).

38 Rajesh, A. *et al.* Skin antigen-presenting cells and wound healing: New knowledge gained and challenges encountered using mouse depletion models. *Immunology* **163**, 98-104, doi:10.1111/imm.13311 (2021).

39 Lachmann, A. *et al.* Massive mining of publicly available RNA-seq data from human and mouse. *Nat Commun* **9**, 1366, doi:10.1038/s41467-018-03751-6 (2018).

40 Zhang, Y. *et al.* Imidazole Ketone Erastin Induces Ferroptosis and Slows Tumor Growth in a Mouse Lymphoma Model. *Cell Chem Biol* **26**, 623-633 e629, doi:10.1016/j.chembiol.2019.01.008 (2019).

41 Keramati, A. R. *et al.* A form of the metabolic syndrome associated with mutations in DYRK1B. *N Engl J Med* **370**, 1909-1919, doi:10.1056/NEJMoa1301824 (2014).

42 Honma, K., Kamikubo, M., Mochizuki, K. & Goda, T. Insulin-induced inhibition of gluconeogenesis genes, including glutamic pyruvic transaminase 2, is associated with reduced histone acetylation in a human liver cell line. *Metabolism* **71**, 118-124, doi:10.1016/j.metabol.2017.03.009 (2017).

43 Nakayasu, E. S. *et al.* Comprehensive Proteomics Analysis of Stressed Human Islets Identifies GDF15 as a Target for Type 1 Diabetes Intervention. *Cell Metab* **31**, 363-374 e366, doi:10.1016/j.cmet.2019.12.005 (2020).

44 Beale, E. G., Harvey, B. J. & Forest, C. PCK1 and PCK2 as candidate diabetes and obesity genes. *Cell Biochem Biophys* **48**, 89-95, doi:10.1007/s12013-007-0025-6 (2007).

45 Thwe, P. M. *et al.* Cell-Intrinsic Glycogen Metabolism Supports Early Glycolytic Reprogramming Required for Dendritic Cell Immune Responses. *Cell Metab* **26**, 558-567 e555, doi:10.1016/j.cmet.2017.08.012 (2017).

46 Zhao, G. *et al.* Delayed wound healing in diabetic (db/db) mice with Pseudomonas aeruginosa biofilm challenge: a model for the study of chronic wounds. *Wound Repair Regen* **18**, 467-477, doi:10.1111/j.1524-475X.2010.00608.x (2010).

47 Bonnefoy, F. *et al.* Factors Produced by Macrophages Eliminating Apoptotic Cells Demonstrate Pro-Resolutive Properties and Terminate Ongoing Inflammation. *Front Immunol* **9**, 2586, doi:10.3389/fimmu.2018.02586 (2018).

48 Pakyari, M., Farrokhi, A., Maharlooei, M. K. & Ghahary, A. Critical Role of Transforming Growth Factor Beta in Different Phases of Wound Healing. *Adv Wound Care (New Rochelle)* **2**, 215-224, doi:10.1089/wound.2012.0406 (2013).

49 Coll, A. P. *et al.* GDF15 mediates the effects of metformin on body weight and energy balance. *Nature* **578**, 444-448, doi:10.1038/s41586-019-1911-y (2020).

50 Patsalos, A., Halasz, L., Medina-Serpas, M. A., Berger, W. K., Daniel, B., Tzerpos, P., Kiss, M., Nagy, G., Fischer, C., Simandi, Z., Varga, T. & Nagy, L. A growth factor-expressing macrophage subpopulation orchestrates regenerative inflammation via GDF-15. *J Exp Med* **219**, doi: 10.1084/jem.20210420 (2021).

**References (Methods)**

51 Deckers, J. *et al.* Co-Activation of Glucocorticoid Receptor and Peroxisome Proliferator-Activated Receptor-gamma in Murine Skin Prevents Worsening of Atopic March. *J Invest Dermatol* **138**, 1360-1370, doi:10.1016/j.jid.2017.12.023 (2018).

52 Sepulveda, F. E. *et al.* Critical role for asparagine endopeptidase in endocytic Toll-like receptor signaling in dendritic cells. *Immunity* **31**, 737-748, doi:10.1016/j.immuni.2009.09.013 (2009).

53 Wiernicki, B. *et al.* Excessive phospholipid peroxidation distinguishes ferroptosis from other cell death modes including pyroptosis. *Cell Death Dis* **11**, 922, doi:10.1038/s41419-020-03118-0 (2020).

54 Hoste, E., Lecomte, K., Annusver, K., Vandamme, N., Roels, J., Maschalidi, S., Verboom, L., Vikkula, H. K., Sze, M., Van Hove, L., Verstaen, K., Martens, A., Hochepied, T., Saeys, Y., Ravichandran, K., Kasper, M. & van Loo, G. OTULIN maintains skin homeostasis by controlling keratinocyte death and stem cell identity. *Nat Commun* **12**, 5913, doi: 10.1038/s41467-021-25944-2 (2021).

55 Sato, H. *et al.* Redox imbalance in cystine/glutamate transporter-deficient mice. *J Biol Chem* **280**, 37423-37429, doi:10.1074/jbc.M506439200 (2005).

56 Van Hove, L. *et al.* Fibrotic enzymes modulate wound-induced skin tumorigenesis. *EMBO Rep* **22**, e51573, doi:10.15252/embr.202051573 (2021).

57 Lambrecht, S. *et al.* Growth differentiation factor 15, a marker of lung involvement in systemic sclerosis, is involved in fibrosis development but is not indispensable for fibrosis development. *Arthritis Rheumatol* **66**, 418-427, doi:10.1002/art.38241 (2014).

58 Hoste, E. *et al.* Innate sensing of microbial products promotes wound-induced skin cancer. *Nat Commun* **6**, 5932, doi:10.1038/ncomms6932 (2015).

59 Van Liefferinge, J. *et al.* Comparative analysis of antibodies to xCT (Slc7a11): Forewarned is forearmed. *J Comp Neurol* **524**, 1015-1032, doi:10.1002/cne.23889 (2016).

809

# Main Figures 1-4 and *Extended Data* 1-10

# Targeting Slc7a11 improves efferocytosis by dendritic cells and diabetic wound healing

Sophia Maschalidi, Parul Mehrotra, Burcu N. Keçeli, Hannah K.L. De Cleene, Kim Lecomte, Renée Van der Cruyssen, Pauline Janssen, Jonathan Pinney, Geert van Loo, Dirk Elewaut, Ann Massie, Esther Hoste, Kodi S. Ravichandran

## Figure Legends

**Fig. 1 | Slc7a11 acts as a break on dendritic cell engulfment of apoptotic cells.**

**a,** Schematic of phagocytosis assays using bone-marrow derived dendritic cells (BMDC) fed apoptotic human Jurkat cells, live cells, or 2µm beads. Histograms illustrate target-derived fluorescence in efferocytic DCs.

**b,c,** Genes associated with transporter activity modulated uniquely after efferocytosis categorized by functionality (**b**), and protein family (**c**). Data are from four independent replicates. ABCs, ATP-binding cassette transporters; GPCRs, G-protein-coupled receptors.

**d,** The SLC7 family gene expression (qRT-PCR) after phagocytosis as in ***a*** above, with *Slc7a5* and *Slc7a11* highlighted (blue). Data represent 3 biological replicates per condition, ****$P < 0.0001$, two-way ANOVA with Sidak's multiple comparison test. ND, not detected

**e,f,** *Slc7a11* siRNA (**e**) or erastin (**f**) increases efferocytosis of apoptotic cells (pHrodo-Green) measured by *Incucyte* live cell imaging. (**e,** $n = 3$ control siRNA, Slc7a11siRNA; $n = 4$ siRNA+CytoD; **f,** $n = 6$ DMSO; $n = 4$ Erastin; $n = 4$ CytoD)

**g,** Schematic of Slc7a11 transport activity and the mice used.

**h,** Kinetics of efferocytosis by Slc7a11 WT and Slc7a11 KO BMDCs treated with erastin or vehicle. Left, $n = 8$ Slc7a11 WT, Slc7a11KO, WT + CytoD; $n = 6$ KO + CytoD; Right, $n = 3$ per condition).

**i,** Efferocytosis of TAMRA- or CypHer5E-labelled apoptotic Jurkat cells compared between control and Slc7a11-null BMDCs (left panels). Purified cDC1 and cDC2 subsets (middle) were tested for phagocytosis with apoptotic and live Jurkat cells at a 1:5 phagocyte:target ratio for 4 hours. Data from $n = 3$-5 biological replicates *$P < 0.05$; **$P < 0.01$; One-way ANOVA with Dunnett's multiple comparisons test.

Floating bars (**d, i,**) show minimum to maximum values with independent replicates, line denotes mean. All live-cell imaging data (**e, f, h**) are expressed as mean ± SEM, ****$P < 0.0001$; One-way ANOVA with Tukey's multiple comparisons test.

**Fig. 2 | Accelerated skin wound healing in the context of Slc7a11 blockade.**

**a,** Hexagonal Tri-wise diagram (left) visualizing relative expression levels of differentially expressed (DE) SLCs (orange) or not (grey) between DCs from lung, spleen and skin. Rose plot (right) depicts the 45 DE genes grouped in bins and by most expressing DC subtype.

**b**, Efferocytosis by dermal phagocytes enriched from the ears of Slc7a11-deficient and control littermates ($n$= 5 per group; * $P$<0.05, unpaired two-tailed $t$-test).

**c,d,** Localization of $CD11c^+$ phagocytes (red) and Slc7a11 (green) in d2 post-wounded skin (**c**) and capturing apoptotic (green) corpses (**d**). Dotted lines: insets. Nuclei: DAPI (blue). Negative control: secondary antibodies. Scale bar: **c,** 10μm **d,** 50μm.

**e**, UMAP clustering of cells isolated from non-lesional (NL) and lesional (L) skin (see Methods) highlighting expression of *Slc7a11*. tSNE plot of cells in lesional skin after scRNAseq analysis (right).

**f,** Gene expression in skin lysates of unwounded ($n$= 3) and wounded mice ($n$= 4) (* $P$<0.05; **** $P$<0.0001, with unpaired two-tailed $t$-test).

**g, j,** Wound healing dynamics of WT mice treated with erastin or vehicle regimen at different stages (**g,** $n$= 8 per group; **j,** $n$=10 vehicle, $n$=9 erastin). Data representative of 4 independent experiments.

**h,i,** H&E-stained wounded skin sections. Scale bars: 100μm (**h**,) Quantification of apoptotic cells in unwounded (UNW $n$ =4-11) and wounded skin ($n$ =10 DMSO; $n$ =11 Erastin regimen) at day 4 post-wounding (** p<0.01 with unpaired $t$-test).

**k,** Healing dynamics comparing Slc7a11 WT and Slc7a11 KO mice ($n$= 6 per group).

**g, j, k,** (* $P$<0.05; *** $P$<0.001; Two-way ANOVA with multiple comparisons)

Box and whiskers (**b, i,**) show minimum to maximum values with all independent replicates, center denotes median and the bounds denote the 25th to 75th percentiles.

**Fig. 3 | Glycolysis and glycogen reserves fuel enhanced efferocytosis.**

**a,** Schematic of RNA-seq analysis of Slc7a11-deficient BMDCs engulfing TAMRA-labelled apoptotic cells for 4 h. $TAMRA^+$ phagocytes (engulfers) were sorted directly into lysis buffer for RNA-seq analysis. The contour plots represent one of four independent experiments.

**b,** Pathway analysis of differentially expressed genes regulated in efferocytic Slc7a11 KO versus WT DCs. Data are from 3-4 independent experimental replicates.

**c,** Glycogen levels in lysates of dendritic cell populations from WT mice treated with erastin or Slc7a11 KO mice. ($n$ = 4, BMDC; $n$ = 3, cDC1) * $P$ <0.05; ** $P$ <0.01; via unpaired two-tailed $t$-test). Results presented as fold change (FC). ns, non-significant.

**d,** Schematic of glycogen metabolism pathway (left). Impact on glycogen levels of BMDC treated with erastin or CP-91149 or both (middle panel; $n$ = 3 per condition; (* p<0.05; ****$p$ < 0.00001. One-way ANOVA with Tukey's multiple comparisons test). Right, Kinetics of efferocytosis after erastin ($n$ = 5), or erastin + CP-91149($n$ = 5). DMSO (vehicle; $n$ = 5 per condition) and CytoD (as negative control; $n$ = 3) are shown.

**e,** Increased glycolytic function in DCs during apoptotic cell clearance and Slc7a11 inhibition. Glycolysis was measured in WT versus Slc7a11 KO or erastin-inhibited dendritic cells at steady state or during efferocytosis. Data represent means ± SEM of $n$= 3 per group; ** $P$<0.01; **** $P$<0.0001; Two-way ANOVA with Tukey's multiple comparisons test). AC: Apoptotic Cells.

**f,** Schematic of aerobic glycolysis pathway with respective inhibitors ($n$ = 4, left; $n$ = 5, right)

**c,d,** Floating bars (**d, i,**) show minimum to maximum values with all independent replicates. All live-cell imaging data (**d, f,**) are expressed as mean ± SEM, ****$P$ < 0.0001; One-way ANOVA with Tukey's multiple comparisons test.

**Fig. 4 | Slc7a11 inhibition and GDF15 promote diabetic skin wound healing.**

**a,** Delayed healing in diabetic mice (*n*=11, *db/db*; *n*=8, B6).

**b,** *Slc7a11* expression in skin lysates from unwounded and wounded (d4) WT (*n*= 6), *db/db* (*n*= 5), and GDF15KO (*n*= 5) mice.

**c, d,** Erastin alone (**c**), and erastin regimen (**d**), accelerate diabetic wound healing. *db/db* mice treated with erastin (*n*= 8) or DMSO (*n*= 7), and the erastin regimen (*n*= 8) or DMSO regimen (*n*= 7). Wound healing of normoglycemic (B6) mice is plotted with dotted lines (*n*= 8). Data represent one of 3 independent experiments.

**e,** Erastin enhances efferocytosis in "diabetic" dendritic cells. Data show ± SEM (*n* = 7 WT, *db/db* DMSO; *n* = 4 WT, *db/db* Erastin, **** *P*< 0.0001. One-way ANOVA; Tukey's multiple comparisons (*db/db* DMSO versus erastin); two-way ANOVA; Sidak's multiple comparisons (WT versus *db/db* DCs).

**f,** Apoptotic cell load in diabetic wounds (*n* =4 per group) (**P*=0.0124; unpaired two-tailed *t*-test).

**g,** Healing dynamics of wild-type mice (*n*=10 per group) treated with sups from efferocytic Slc7a11KO and control DCs.

**h,** (left) Heatmap of TGFβ superfamily genes. Data presented as z-score from three independent experimental replicates. (right) GDF-15 secretion by DCs 12hr after incubation with apoptotic targets (*n*=4 per condition), or by targets alone (*n*=3).

**i,** GDF15 levels in unwounded (*n*=2, B6; *n*=5 *db/db*) and wounded skin lysates (*n*=3-4, B6; *n*=3 *db/db*).

**j,** Wound size comparing GDF15KO and littermate control mice (*n*= 16 per group, ** *P*<0.01, via unpaired two-tailed *t*-test).

**k,** Topical administration of recGDF15 (*n*= 11) improves diabetic healing.

**a,c,d,g,k** Data represent means ± SEM.(* *P*<0.05; ** *P*<0.01; **** *P*<0.0001Two-way ANOVA with multiple comparisons)

**h, i,** **P* < 0.05; ***P* < 0.001; One-way ANOVA with Tukey's multiple comparisons test.

Violin plots (**b,f,i,**), and the box and whiskers plots (**g,h,j**) show the minimum to maximum values with all independent replicates, center denotes median.

**Extended data 1 | Analyzing amino acid transporters during dendritic cell efferocytosis.**

**a,** SLC programs modulated in dendritic cells during efferocytosis of apoptotic cells compared to sterile phagocytosis. RNAseq was performed on primary BMDCs after engulfment apoptotic human Jurkat cells or beads. The heatmap illustrates SLCs upregulated and downregulated during dendritic cell efferocytosis.

**b,** Uptake of CypHer5E- labelled apoptotic Jurkat cells by dendritic cells (BMDC) silenced for *Slc7a1* expression ($n$ = 2 per condition).

**c,** *Slc7a5* siRNA targeting in dendritic cells does not significantly affect apoptotic cell uptake as assessed by Incucyte Live-cell imaging ($n$ = 4 per group).

**d,** Efferocytosis of TAMRA-labelled apoptotic Jurkat cells by dendritic cells treated with different concentrations of the Slc7a5 inhibitor, JPH-203 ($n$= 2 per condition).

**e,** Kinetics of efferocytosis by BMDC treated with 3μM JPH-203 ($n$ = 3 per condition).

**f,** Measurement of degradation of TAMRA (pH insensitive) and Cell Trace Violet (pH sensitive) co-labelled apoptotic targets after efferocytosis by Slc7a11 KO and WT dendritic cells ($n$ = 4 per group). Dendritic cells were incubated with apoptotic targets at a 1:5 phagocyte:target ratio for four hours. Floating bars show minimum to maximum values with all independent replicates, line denotes mean.

**g,** Kinetics of efferocytosis by Slc7a11 WT and Slc7a11 KO bone marrow-derived macrophages with or without erastin treatment ($n$ = 4 per group). ns: not significant; via One-way ANOVA with Tukey's multiple comparisons test.

**h,** Efferocytosis by peritoneal macrophages after Slc7a11 inhibition via erastin. ($n$= 8 per condition; $P$= 0.19, with paired, two-tailed $t$-test).

**c,e,g,** All live-cell imaging data are expressed as mean ± SEM.

**Extended data 2 | Ferroptosis inducer and DC efferocytosis.**

**a,** Phagocytosis of E. *coli* bioparticles by dendritic cells measured at different time points with or without erastin treatment. Data are expressed as mean ± SD with $n = 2$ per condition.

**b,** Ferroptosis inducer ML-162 does not enhance efferocytosis by dendritic cells. Live-cell imaging data are expressed as mean ± SEM ($n = 3$, DMSO and CytoD; $n = 4$, ML-162; $n = 6$, Erastin)

**c,** Kinetics of efferocytosis by dendritic cells treated with antioxidant, Ferrostatin-1, erastin alone, or erastin + Ferrostatin-1 ($n = 4$ per condition, data are representative of two independent experiments).

**d,** Measurement of glutathione levels in dendritic cells treated with erastin ($n = 3$ per condition, *** $P < 0.001$; via unpaired two-tailed *t*-test).

**e,** Assessment of erastin drug cytotoxicity in dendritic cells by measuring Sytox Green fluorescence. Data are expressed as mean ± SD with $n = 2$ per condition.

**f,** Measurement of lipid peroxidation and ROS (via C11-BODIPY and dihydrorhodamine 123 probes, respectively) in dendritic cells treated with ferroptosis inducers ($n = 3$ per condition). Results are expressed as fold change (FC).

**g,** Direct comparison of kinetics of efferocytosis by dendritic cells treated with glutamate or erastin ($n = 4$, Glutamate and Erastin; $n = 8$, DMSO).

**h,** Kinetics of efferocytosis after NAC, erastin alone or erastin + NAC treatment. DMSO was used as a vehicle control ($n = 7$, per condition).

All live-cell imaging data (**b, c, g, h,**) are expressed as mean ± SEM, * $P<0.05$ *** $P<0.001$; **** $P<0.0001$; One-way ANOVA with Tukey's multiple comparisons test. ns: non-significant

**Extended data 3 | Contribution of GSH and ROS in the context of enhanced efferocytosis by Slc7a11KO/inhibition.**

**a, b,** GSH supplementation or depletion does not affect the enhanced efferocytosis by DCs lacking Slc7a11 or treated with erastin. WT ($n$ = 6) and Slc7a11 KO ($n$ = 6) dendritic cells were supplemented with different concentrations of reduced GSH ($n$ = 3 per concentration) (**a**), or treated with glutathione reducing compound, BSO (50μM), erastin or erastin + BSO (**b**) ($n$ = 3 per condition). DMSO was used as a vehicle control. Data are representative of 4 or 6 independent experiments,

**c, d,** Interfering with ROS may be a component but is not sufficient to reverse the enhanced efferocytosis by Slc7a11 inhibited DCs.

**c,** WT DCs were treated with 1μM FCCP, together with erastin, erastin or DMSO alone ($n$ = 7 per condition) or

**d,** WT DCs were treated with mitoTEMPO (100μM; $n$ = 4) for ameliorating and scavenging ROS respectively, together with erastin ($n$ = 4) or erastin alone ($n$ = 4). DMSO was used as a vehicle control ($n$ = 3). Data are representative of three or five independent experiments.

All live-cell imaging data are expressed as mean ± SEM ($P$=0.067, **$P$<0.01, ****$P$ < 0.0001; ns: non-significant; One-way ANOVA with Tukey's multiple comparisons test).

**Extended data 4 | Analysis of dermal DCs and wound healing.**

**a,** Gating strategy of enriched phagocytes after digestion of ears and depletion of lymphocytes.

**b,** Immunofluorescent images of skin sections from unwounded PDGFR-GFP mice depicting Slc7a11-positive (red) cells. Nuclei were stained with DAPI. Scale bar: 50 μm.

**c,** Annotations of innate immune cell populations arising in lesional skin.

**d,** Frequencies of *Slc7a11* expression in innate immune cells of lesional and non-lesional skin.

**e,** Representative images of wounds of mice treated with erastin or vehicle at day 10 post-wounding.

**f,** Wound healing dynamics comparing WT mice after full-thickness wounding and a single topical administration of apoptotic targets at the day of wounding or erastin and vehicle only at day 0 till day 2 ($n$= 8 per group). Data represent means ± SEM.

**g,** Comparison of wound closure at day 2 post wounding in WT mice treated with RSL3 regimen ($n$=9) versus erastin regimen ($n$=7) or DMSO regimen ($n$=7). Data represent means ± SEM.* $P$<0.05; ** $P$<0.01. One-way ANOVA with Tukey's multiple comparisons test). Box and whiskers show minimum to maximum values with all independent replicates, center denotes median.

**h, i,** Erastin regimen promotes *in vivo* migration of keratinocytes during wound healing. PDGFRa-H2BeGFP mice were treated with erastin or DMSO regimen after full-thickness wounding with an 8 mm punch biopsy. Skin sections at day 4 post-wounding were stained with **h,** Itga5 ($n$=4 per condition, keratinocytes; $n$=4 DMSO-fibroblasts; $n$=7 Erastin-fibroblasts) or **i,** Ki67 ($n$ =4 per condition, keratinocytes; $n$=4 DMSO-fibroblasts; $n$=5 Erastin-fibroblasts) Quantification (right) and representative immunofluorescent images (left) of skin sections with respective treatments. Nuclei were stained with DAPI (blue). Violins plots show minimum to maximum values with all independent replicates, centre denotes median. (*$P$=0.0420; unpaired two-tailed $t$-test); ns:not-significant. Scale bar: 150 μm.

**j,** Percentage of scratch wound closure (re-epithelialization) of mouse primary Slc7a11 WT ($n$=5) and KO ($n$=4) keratinocytes pretreated with mitomycin C. Slc7a11KO keratinocytes show no difference indicating that the effect on migration *in vivo* (**h**) is not cell intrinsic. Data are expressed as mean ± SD.

**Extended data 5 | Gene expression patterns in Slc7a11 KO efferocytic dendritic cells.**

**a,** Heat maps comparing efferocytic Slc7a11 KO versus WT dendritic cells showing upregulation and downregulation of differentially expressed genes ($0.58 \leq Log2FC \leq -0.58$) that are associated with metabolic and mitochondrial function, protein synthesis, ER homeostasis, transcription regulation, signaling, wound healing, cell cycle, migration and other transporters. Data are from 3-4 independent experimental replicates. *Gdf15* falls under the transcriptional programs of metabolic function and regeneration, and is highlighted in red.

**Extended data 6 | Glycogen pools are altered in the absence of Slc7a11 and affect DC efferocytosis.**

**a,** Schematic of glycogen metabolism pathway indicating the enzymes involved in glycogen breakdown, degradation and synthesis. In box, it is illustrated the inhibitory phosphorylation of Ser641, Ser645 and Ser649 on Gys1 which leads to decreased glycogen synthesis.

**b,** *Pygl* siRNA targeting in dendritic cells compromises enhanced efferocytosis of Slc7a11-inhibited DCs. Live-cell imaging are expressed as mean ± SEM with $n$=4 per condition, and are representative of two independent experiments. *$P$<0.05; One-way ANOVA with Tukey's multiple comparisons test.

**c, d,** PYG inhibition via DAB compromises enhanced efferocytosis of Slc7a11-inhibited (**c**) or Slc7a11-KO DCs (**d**). Live-cell imaging are expressed as mean ± SEM with $n$=3 per condition, and are representative of two independent experiments. ****$P$<0.0001; One-way ANOVA with Tukey's multiple comparisons test.

**e, f,** Representative immunoblot (**e**) and quantification of glycogen metabolism enzymes (**f**). Data are expressed as fold change (FC) of erastin-treated BMDC to DMSO control with $n$=14;Pygl and $n$=13;Agl, Gys1, pGys1; **$P$ < 0.01; ***$P$< 0.001, ns: non-significant via paired, two-tailed $t$-test.

**Extended data 7 | Metabolic inhibitors and DC efferocytosis.**

**a,** Increased aerobic glycolysis in dendritic cells during apoptotic cell clearance and Slc7a11 inhibition. Glycolysis and OXPHOS were measured at resting dendritic cells or during efferocytosis using Seahorse XF via extracellular acidification rate (ECAR) and oxygen consumption rate (OCR). Data represent means ± SEM of $n$=4 per group; * $P$<0.05; ** $P$<0.01; *** $P$<0.001; **** $P$<0.0001 via unpaired, two-tailed $t$-test or Two-way ANOVA with Tukey's multiple comparisons test. AC: Apoptotic Cells.

**b,** Spare capacity was measured in dendritic cells after vehicle or erastin-treatment or during efferocytosis (with Seahorse XF) using oxygen consumption rate (OCR). Data from $n$=4 per group; * $P$<0.05; ** $P$<0.01; *** $P$<0.001, via One-way ANOVA with Tukey's multiple comparisons test. AC: Apoptotic Cells.

Box and whiskers (**a,b,**) show minimum to maximum values with all independent replicates, center denotes median.

**c,** Assessment of cytotoxicity of drugs tested on dendritic cells by measuring Sytox Green fluorescence $n$=4; DMSO, 2-DG, 3-BP; $n$=2; UK5099, DON.

**d,** Kinetics of efferocytosis by WT BMDC treated with the indicated inhibitors DON ($n$=3; DMSO, Erastin, DON, DON+ Erastin) or UK5099 ($n$=3; DMSO, Erastin, UK5099, UK5099+ Erastin) or CB-839 ($n$=3; DMSO, CB-839; $n$=6; Erastin, CB-839+ Erastin) (see schematic representation) alone or in combination with erastin. DMSO was used as a vehicle control. All live-cell imaging data are expressed as mean ± SEM and are representative of four independent experiments (*$P$<0.05; ***$P$<0.001; ns: not significant via One-way ANOVA with Tukey's multiple comparisons test).

**Extended data 8 | Glycolysis/glycogen pathway inhibitors and wound healing.**

**a,** Co-administration of CP-91149 or 3-BP with erastin regimen can reverse the accelerated wound healing in the context of Slc7a11 blockade. Wound healing dynamics of wild-type mice treated with erastin regimen or vehicle regimen consisting of a single administration to the wound site of apoptotic cells at day 0 along with erastin or DMSO vehicle given on day 0 to day 2. When indicated, the compounds CP-91149 and 3-BP were topically administered on the wounds, on day 0 to day 2. Data represent means ± SEM and show one out of two independent experiments with $n$=9; DMSO regimen, $n$=10; Erastin regimen, $n$=8; DMSO regimen + CP-91149 or 3-BP, $n$=8; Erastin regimen + CP-91149 or 3-BP (* $P$<0.05; **** $P$<0.0001 via Two-way ANOVA with Tukey's multiple comparisons test).

**Extended data 9 | Targeted metabolomics profiling in Slc7a11-null or inhibited DC.**

**a,** Peak intensity of several metabolites (absolute concentrations via targeted metabolomics) in the pellet of WT, Slc7a11 KO, and erastin-treated dendritic cells at steady state or upon efferocytosis ($n$= 4 biological replicates per condition; ****$P$<0.0001 via One-way ANOVA with Tukey's multiple comparisons test). Box and whiskers show minimum to maximum values with all independent replicates, center denotes median.

**Extended data 10 | Erastin ameliorates corpse clearance in the wounds of *db/db* mice and promotes partial wound healing in GDF15 KO mice.**

**a, b,** Erastin ameliorates corpse clearance with or without the addition of apoptotic bolus in in the wounds of *db/db* mice. Quantification of apoptotic cleaved caspase-$3^+$ cells in wounded skin of **a,** normoglycemic (B6) mice at day 4 post-wounding and **b,** diabetic (*db/db*) mice at day 8 post-wounding treated with erastin or vehicle regimen versus erastin or DMSO (for vehicle control) without the single administration of the apoptotic bolus. (B6: $n$=4; UNW; $n$=10; Vehicle regimen; $n$=11; Erastin regimen; $n$=4; Vehicle or Erastin; *db/db*: $n$=5 mice per group; * $P$<0.05; ** $P$<0.01 with unpaired, two-tailed $t$-test).

**c,** Lysates were prepared using bone-marrow derived dendritic cells from WT, GDF15 KO and Slc7a11 KO mice, mRNA was isolated, followed by RT-qPCR analysis for *Slc7a11*. ($n$= 5 per genotype; data are presented as fold change to *Slc7a11* expression to control (WT) BMDC).

**d,** GDF15 deficiency does not impair DC efferocytosis. Kinetics of efferocytosis by GDF15 KO and WT BMDC. Live-cell imaging data are expressed as mean ± SEM with $n$=12; WT, $n$=8; GDF15KO.

**e,** Erastin regimen promotes partial wound healing in GDF15 KO mice. Wound healing dynamics comparing GDF15 KO and littermate control mice treated with erastin or DMSO vehicle given on day 0 to day 2. All wound sizes are expressed as percentage of initial wound size at day 2 post-wounding. ($n$=8; WT+Erastin, $n$=9; WT+vehicle, KO+Vehicle, KO+Erastin; * $P$<0.05; ** $P$<0.01; between groups, via unpaired, two-tailed $t$-test.

Violin plots (**c,**), and the box and whiskers plots (**a,b,e**) show the minimum to maximum values with all independent replicates, center denotes median.

**Extended data Table 1 | Top 10 predictions for Slc7a11 associated diseases via ARCHS[4].**

The predictions were derived from mining of publicly available RNA-seq data from human and mouse via ARCHS[4] database.

Figure 1

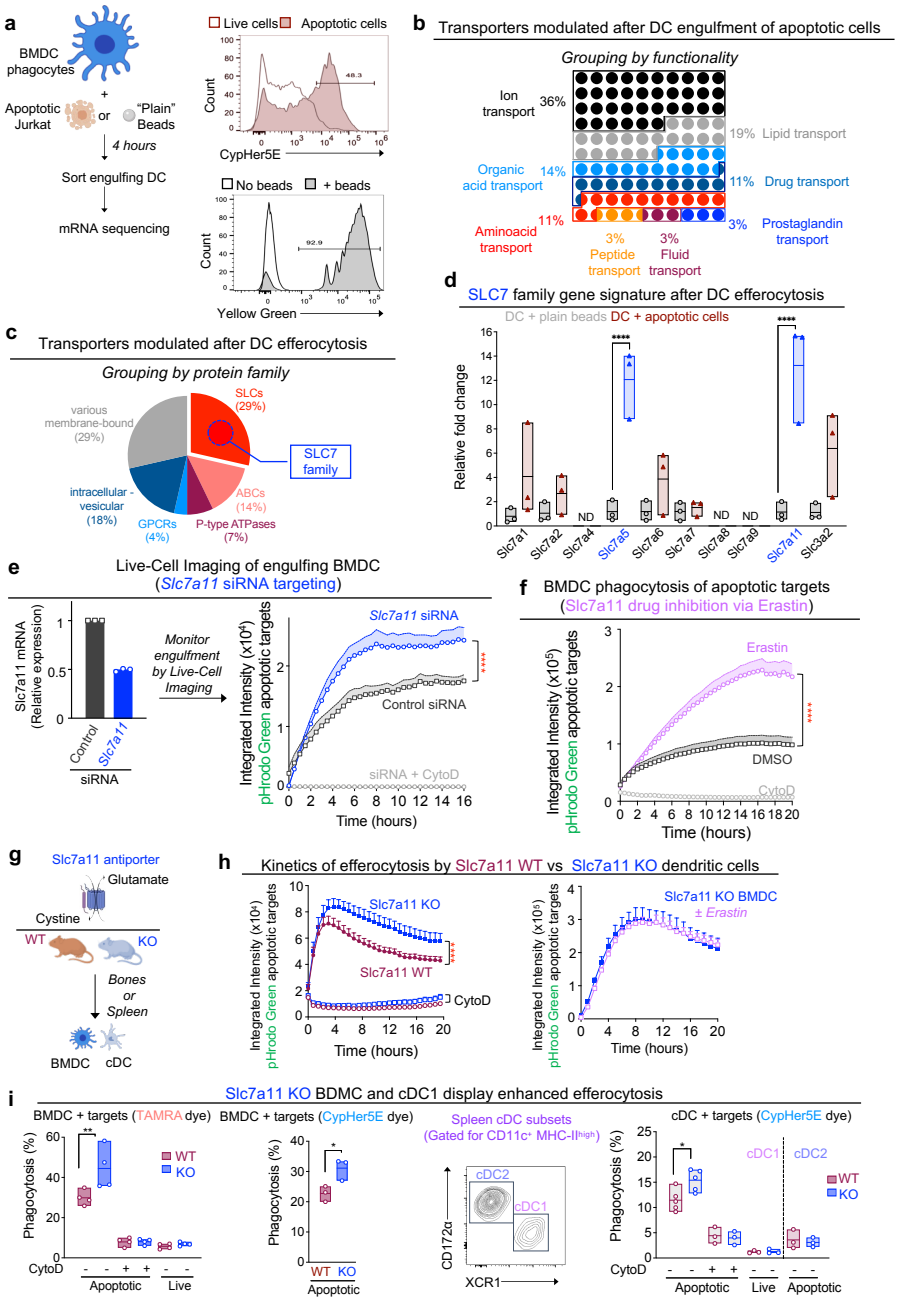
a
BMDC phagocytes
+
Apoptotic Jurkat
or
"Plain" Beads
4 hours
Sort engulfing DC
mRNA sequencing
Live cells
Apoptotic cells
Count
CypHer5E
No beads
+ beads
Yellow Green
b
Transporters modulated after DC engulfment of apoptotic cells
Grouping by functionality
Ion transport 36%
Organic acid transport 14%
Aminoacid transport 11%
3% Peptide transport
3% Fluid transport
3% Prostaglandin transport
11% Drug transport
19% Lipid transport
c
Transporters modulated after DC efferocytosis
Grouping by protein family
SLCs (29%)
SLC7 family
ABCs (14%)
P-type ATPases (7%)
GPCRs (4%)
intracellular vesicular (18%)
various membrane-bound (29%)
d
SLC7 family gene signature after DC efferocytosis
DC + plain beads
DC + apoptotic cells
Relative fold change
Slc7a1
Slc7a2
Slc7a4
Slc7a5
Slc7a6
Slc7a7
Slc7a8
Slc7a9
Slc7a11
Slc3a2
ND
e
Live-Cell Imaging of engulfing BMDC
(Slc7a11 siRNA targeting)
Slc7a11 mRNA (Relative expression)
Control
Slc7a11
siRNA
Monitor engulfment by Live-Cell Imaging
Integrated Intensity (x10⁶) pHrodo Green apoptotic targets
Slc7a11 siRNA
Control siRNA
siRNA + CytoD
Time (hours)
f
BMDC phagocytosis of apoptotic targets
(Slc7a11 drug inhibition via Erastin)
Integrated Intensity (x10⁵) pHrodo Green apoptotic targets
Erastin
DMSO
CytoD
Time (hours)
g
Slc7a11 antiporter
Glutamate
Cystine
WT
KO
Bones or Spleen
BMDC
cDC
h
Kinetics of efferocytosis by Slc7a11 WT vs Slc7a11 KO dendritic cells
Integrated Intensity (x10⁵) pHrodo Green apoptotic targets
Slc7a11 KO
Slc7a11 WT
CytoD
Time (hours)
Slc7a11 KO BMDC
± Erastin
i
Slc7a11 KO BMDC and cDC1 display enhanced efferocytosis
BMDC + targets (TAMRA dye)
BMDC + targets (CypHer5E dye)
Spleen cDC subsets
(Gated for CD11c⁺ MHC-II^high)
cDC + targets (CypHer5E dye)
Phagocytosis (%)
WT
KO
CytoD
Apoptotic
Live
cDC2
cDC1
CD172a
XCR1

Figure 2

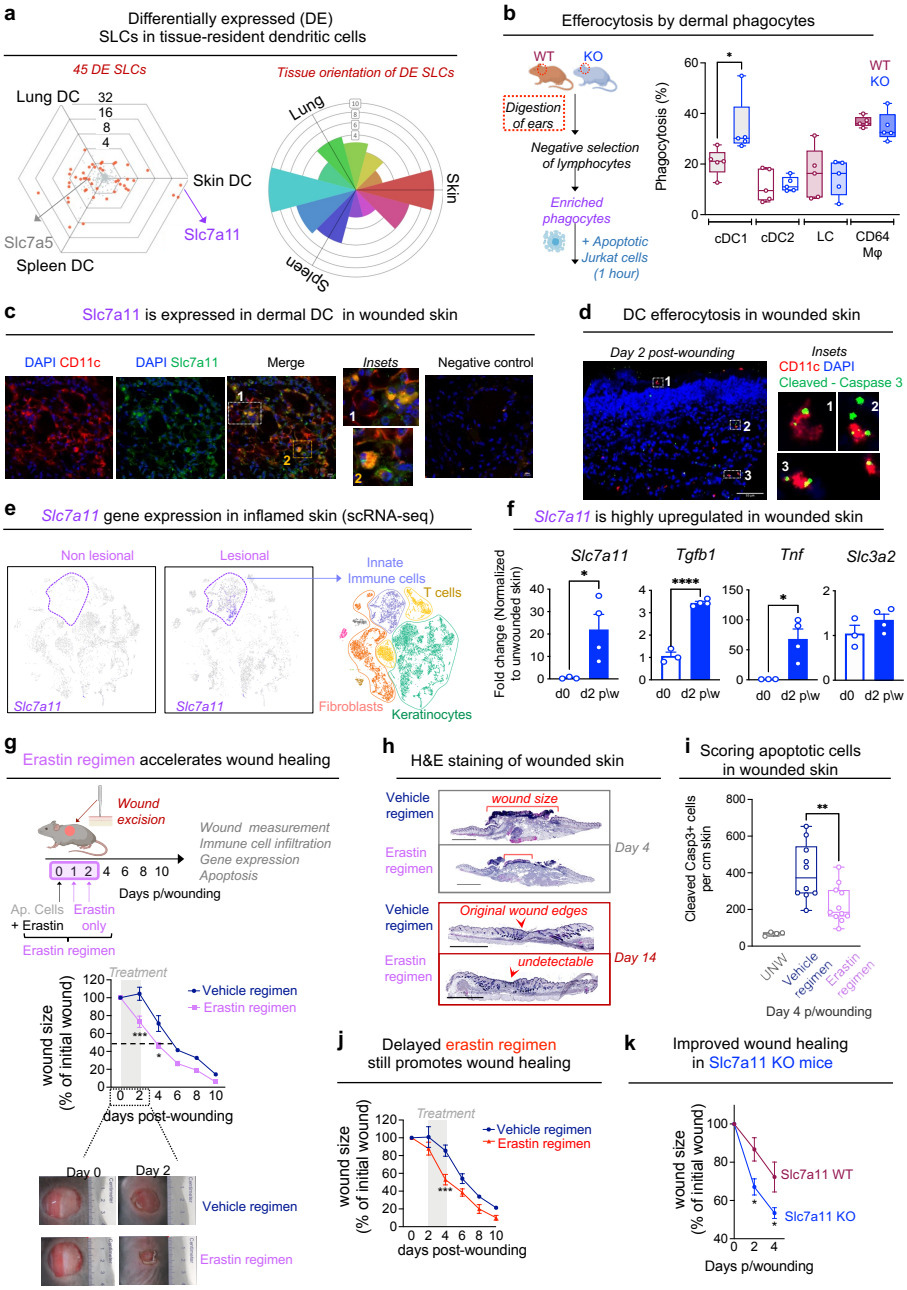
a
Differentially expressed (DE) SLCs in tissue-resident dendritic cells
45 DE SLCs
Tissue orientation of DE SLCs
Lung DC
Skin DC
Slc7a11
Slc7a5
Spleen DC
Lung
Skin
Spleen
b
Efferocytosis by dermal phagocytes
WT
KO
Digestion of ears
Negative selection of lymphocytes
Enriched phagocytes
+ Apoptotic Jurkat cells (1 hour)
Phagocytosis (%)
cDC1
cDC2
LC
CD64 Mφ
c
Slc7a11 is expressed in dermal DC in wounded skin
DAPI CD11c
DAPI Slc7a11
Merge
Insets
Negative control
d
DC efferocytosis in wounded skin
Day 2 post-wounding
Insets
CD11c DAPI
Cleaved - Caspase 3
e
Slc7a11 gene expression in inflamed skin (scRNA-seq)
Non lesional
Lesional
Innate Immune cells
T cells
Fibroblasts
Keratinocytes
Slc7a11
f
Slc7a11 is highly upregulated in wounded skin
Slc7a11
Tgfb1
Tnf
Slc3a2
Fold change (Normalized to unwounded skin)
d0
d2 p\w
g
Erastin regimen accelerates wound healing
Wound excision
Wound measurement
Immune cell infiltration
Gene expression
Apoptosis
Days p/wounding
Ap. Cells + Erastin
Erastin only
Erastin regimen
Treatment
Vehicle regimen
Erastin regimen
wound size (% of initial wound)
days post-wounding
Day 0
Day 2
h
H&E staining of wounded skin
Vehicle regimen
Erastin regimen
wound size
Day 4
Original wound edges
undetectable
Day 14
i
Scoring apoptotic cells in wounded skin
Cleaved Casp3+ cells per cm skin
UNW
Vehicle regimen
Erastin regimen
Day 4 p/wounding
j
Delayed erastin regimen still promotes wound healing
Treatment
Vehicle regimen
Erastin regimen
wound size (% of initial wound)
days post-wounding
k
Improved wound healing in Slc7a11 KO mice
Slc7a11 WT
Slc7a11 KO
wound size (% of initial wound)
Days p/wounding

Figure 3

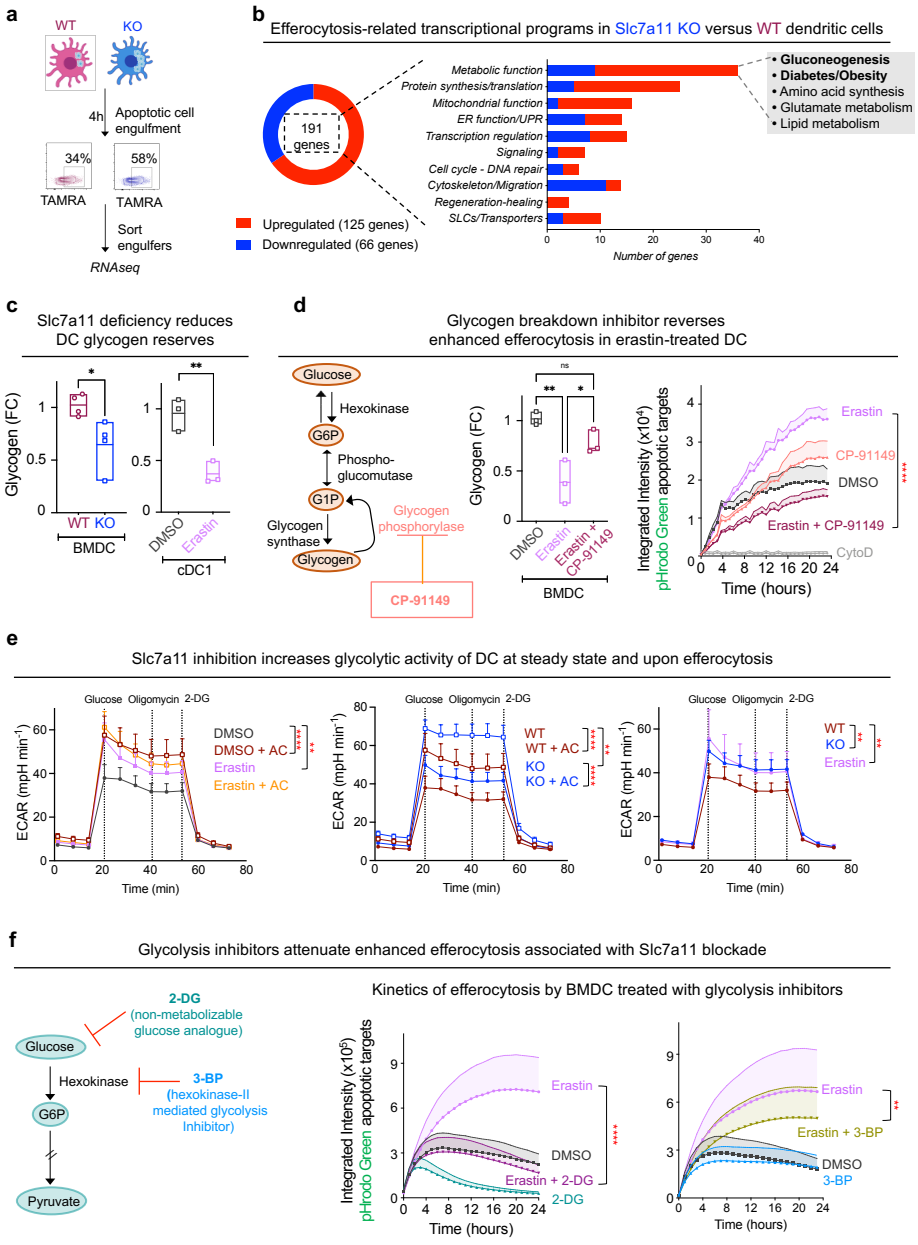
a
WT
KO
4h
Apoptotic cell engulfment
34%
58%
TAMRA
TAMRA
Sort engulfers
RNAseq
b
Efferocytosis-related transcriptional programs in Slc7a11 KO versus WT dendritic cells
191 genes
Upregulated (125 genes)
Downregulated (66 genes)
Metabolic function
Protein synthesis/translation
Mitochondrial function
ER function/UPR
Transcription regulation
Signaling
Cell cycle - DNA repair
Cytoskeleton/Migration
Regeneration-healing
SLCs/Transporters
Number of genes
• Gluconeogenesis
• Diabetes/Obesity
• Amino acid synthesis
• Glutamate metabolism
• Lipid metabolism
c
Slc7a11 deficiency reduces DC glycogen reserves
Glycogen (FC)
WT KO
BMDC
DMSO
Erastin
cDC1
d
Glycogen breakdown inhibitor reverses enhanced efferocytosis in erastin-treated DC
Glucose
Hexokinase
G6P
Phospho-glucomutase
G1P
Glycogen synthase
Glycogen
Glycogen phosphorylase
CP-91149
Glycogen (FC)
DMSO
Erastin
Erastin + CP-91149
BMDC
Integrated Intensity (x10⁴) pHrodo Green apoptotic targets
Erastin
CP-91149
DMSO
Erastin + CP-91149
CytoD
Time (hours)
e
Slc7a11 inhibition increases glycolytic activity of DC at steady state and upon efferocytosis
Glucose
Oligomycin
2-DG
ECAR (mpH min⁻¹)
Time (min)
DMSO
DMSO + AC
Erastin
Erastin + AC
WT
WT + AC
KO
KO + AC
f
Glycolysis inhibitors attenuate enhanced efferocytosis associated with Slc7a11 blockade
2-DG
(non-metabolizable glucose analogue)
Glucose
Hexokinase
3-BP
(hexokinase-II mediated glycolysis Inhibitor)
G6P
Pyruvate
Kinetics of efferocytosis by BMDC treated with glycolysis inhibitors
Integrated Intensity (x10⁶) pHrodo Green apoptotic targets
Erastin
DMSO
Erastin + 2-DG
2-DG
Time (hours)
Erastin
Erastin + 3-BP
DMSO
3-BP
Time (hours)

Figure 4

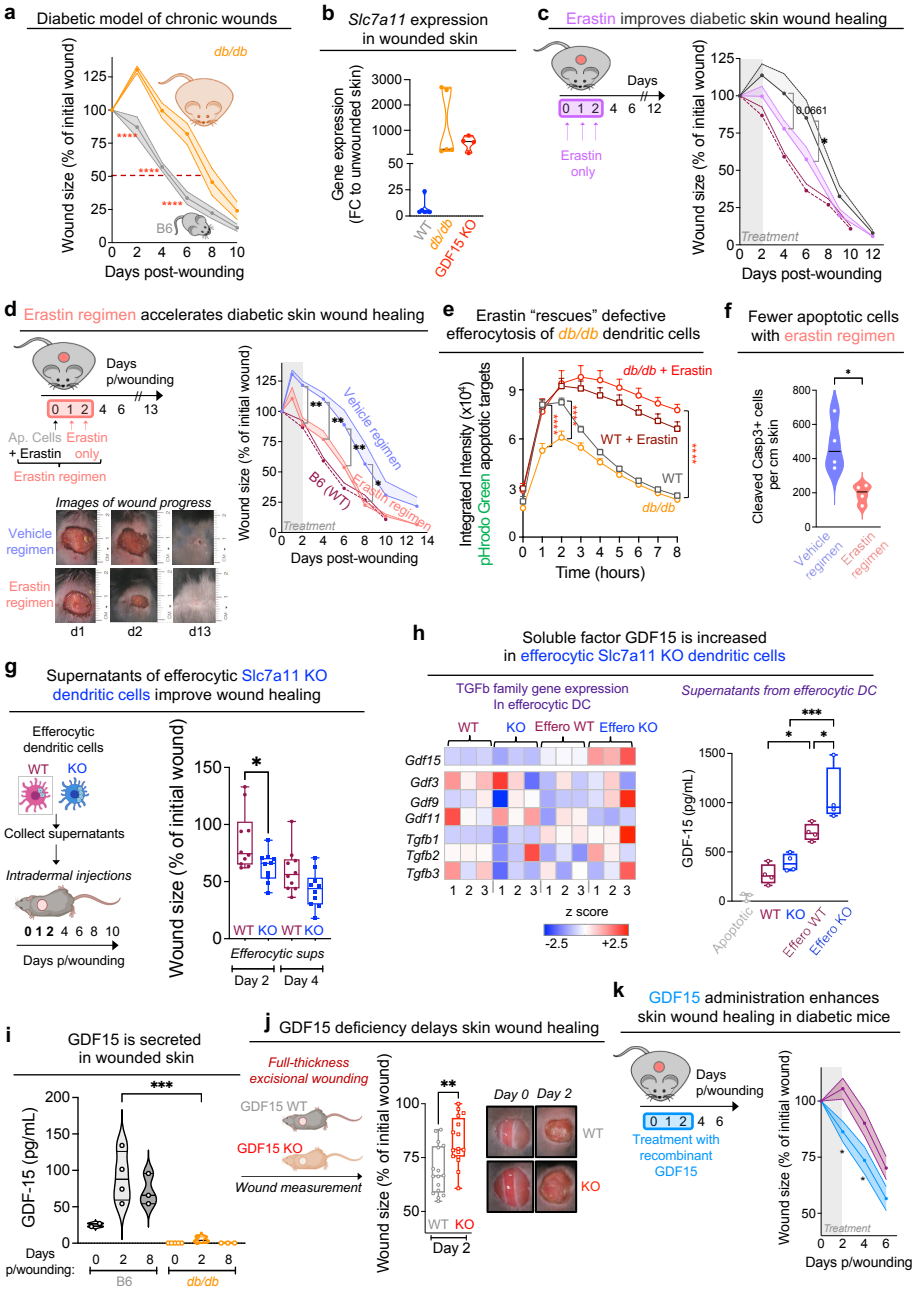
a
Diabetic model of chronic wounds
db/db
B6
Wound size (% of initial wound)
Days post-wounding
b
Slc7a11 expression in wounded skin
Gene expression (FC to unwounded skin)
WT
db/db
GDF15 KO
c
Erastin improves diabetic skin wound healing
Days
Erastin only
Treatment
Wound size (% of initial wound)
Days post-wounding
d
Erastin regimen accelerates diabetic skin wound healing
Days p/wounding
Ap. Cells + Erastin
Erastin only
Erastin regimen
Images of wound progress
Vehicle regimen
Erastin regimen
d1
d2
d13
Vehicle regimen
B6 (WT)
Erastin regimen
Treatment
Wound size (% of initial wound)
Days post-wounding
e
Erastin "rescues" defective efferocytosis of db/db dendritic cells
db/db + Erastin
WT + Erastin
WT
db/db
Integrated Intensity (x10³) pHrodo Green apoptotic targets
Time (hours)
f
Fewer apoptotic cells with erastin regimen
Cleaved Casp3+ cells per cm skin
Vehicle regimen
Erastin regimen
g
Supernatants of efferocytic Slc7a11 KO dendritic cells improve wound healing
Efferocytic dendritic cells
WT
KO
Collect supernatants
Intradermal injections
Days p/wounding
Wound size (% of initial wound)
WT KO WT KO
Efferocytic sups
Day 2
Day 4
h
Soluble factor GDF15 is increased in efferocytic Slc7a11 KO dendritic cells
TGFb family gene expression In efferocytic DC
WT
KO
Effero WT
Effero KO
Gdf15
Gdf3
Gdf9
Gdf11
Tgfb1
Tgfb2
Tgfb3
z score
-2.5
+2.5
Supernatants from efferocytic DC
GDF-15 (pg/mL)
Apoptotic
WT
KO
Effero WT
Effero KO
i
GDF15 is secreted in wounded skin
GDF-15 (pg/mL)
Days p/wounding:
B6
db/db
j
GDF15 deficiency delays skin wound healing
Full-thickness excisional wounding
GDF15 WT
GDF15 KO
Wound measurement
Wound size (% of initial wound)
Day 2
Day 0
Day 2
WT
KO
k
GDF15 administration enhances skin wound healing in diabetic mice
Days p/wounding
Treatment with recombinant GDF15
Treatment
Wound size (% of initial wound)
Days p/wounding

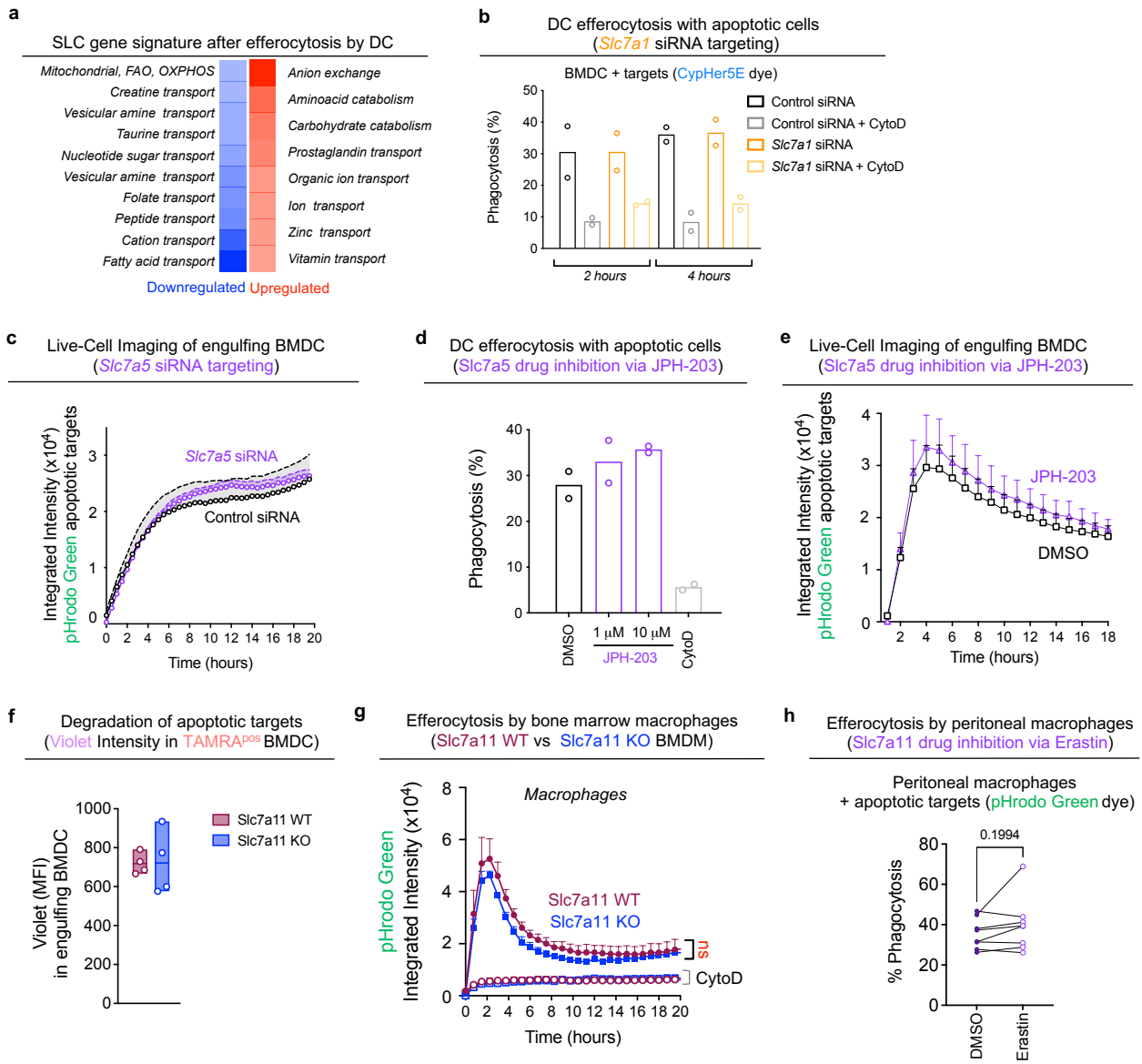


**Extended data Figure 1 Analyzing amino acid transporters during efferocytosis.**

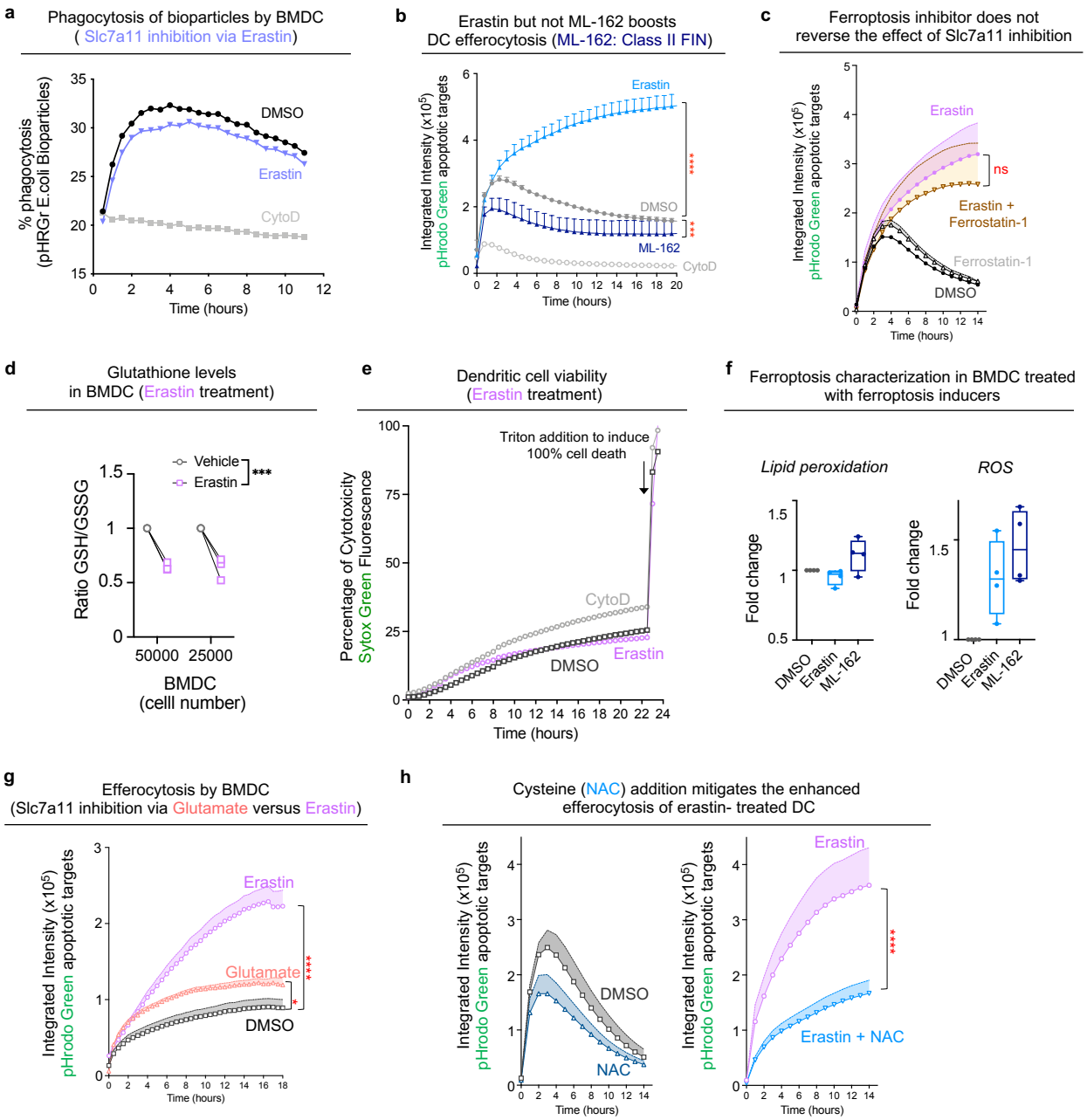


**Extended data Figure 2. Ferroptosis inducers and DC efferocytosis.**

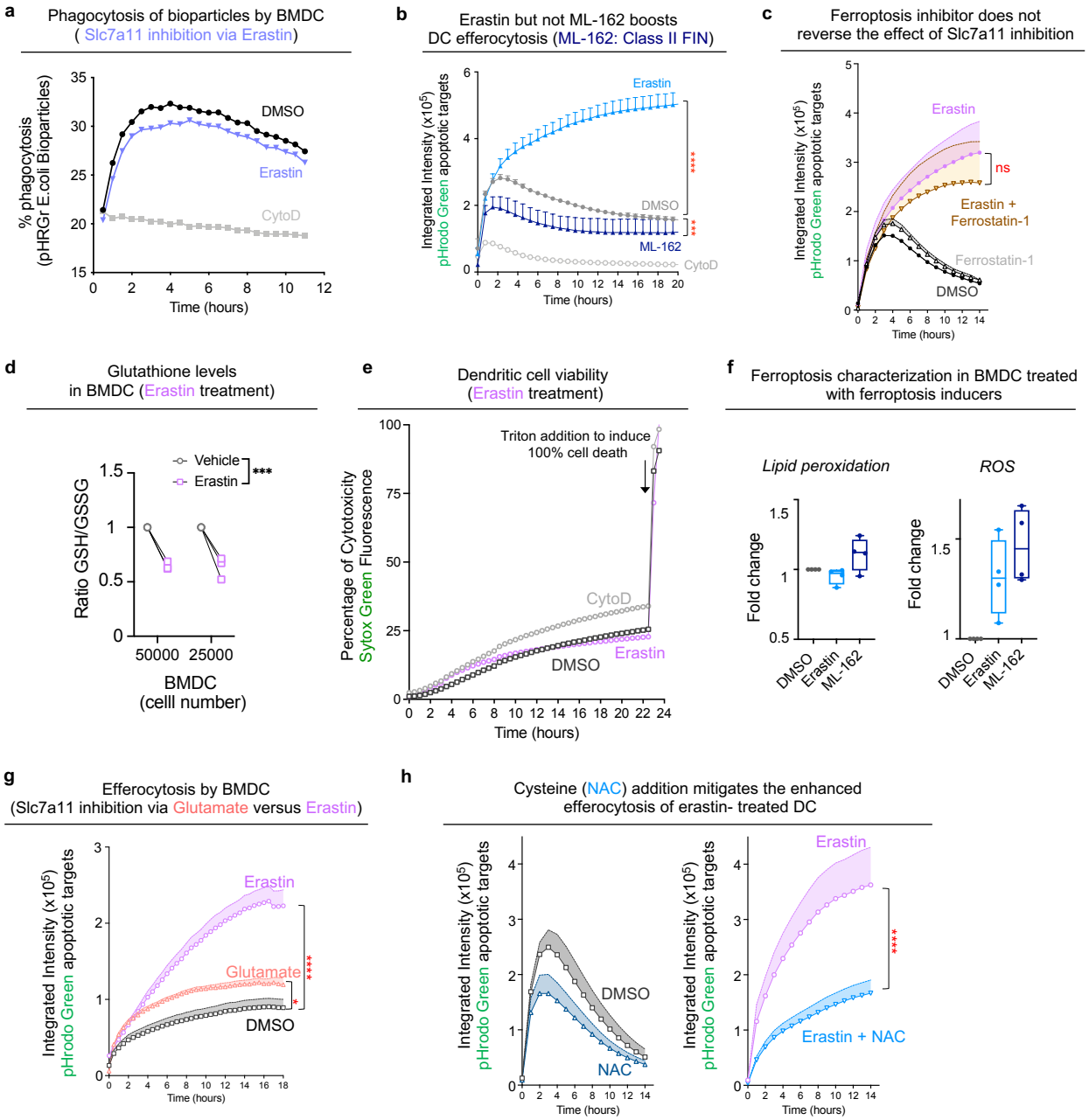


**Extended data Figure 2. Ferroptosis inducers and DC efferocytosis.**

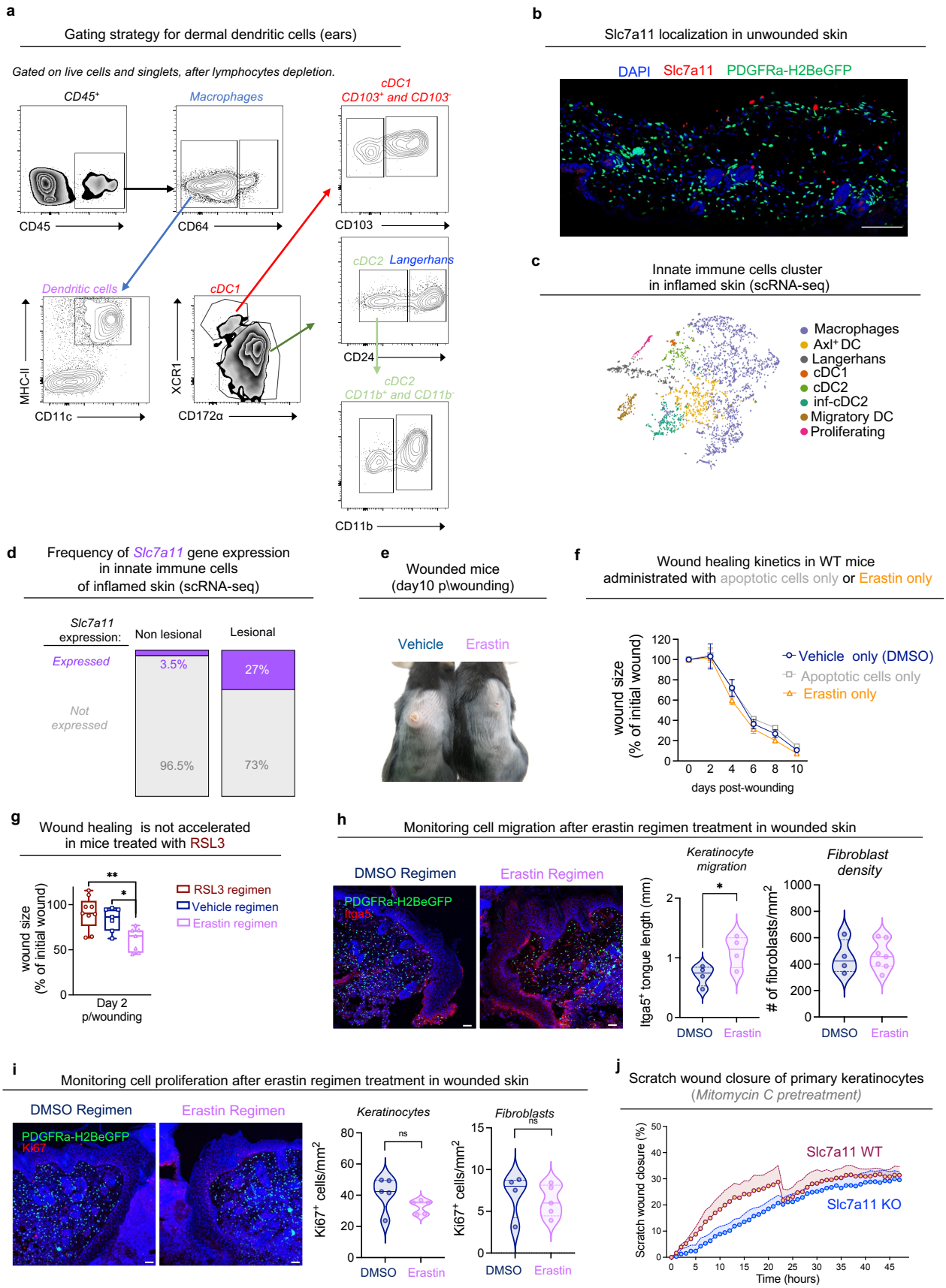


**Extended data Figure 4. Analysis of dermal DCs and wound healing.**

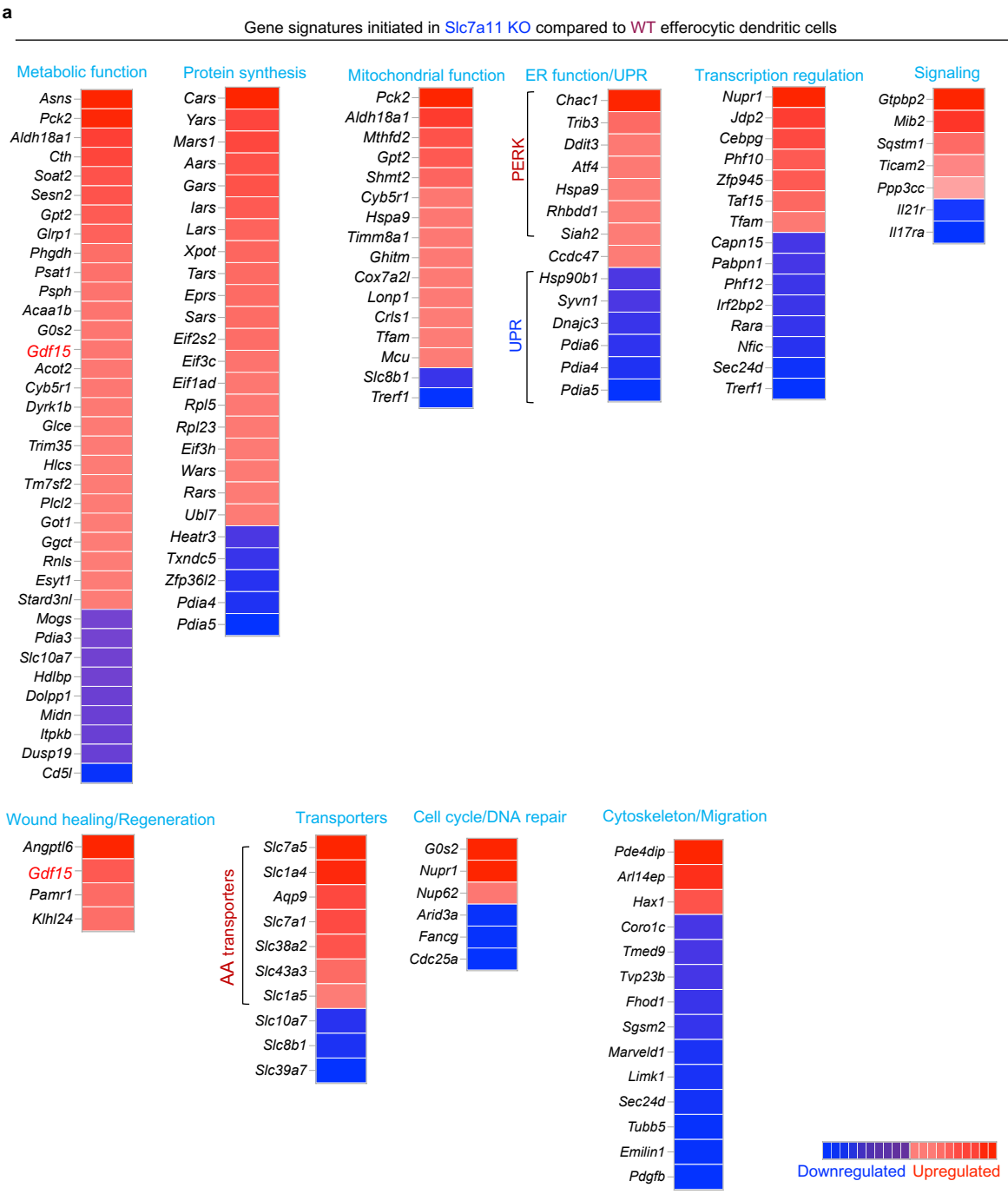


**Extended data Figure 5. Gene expression patterns in Slc7a11 KO efferocytic dendritic cells.**

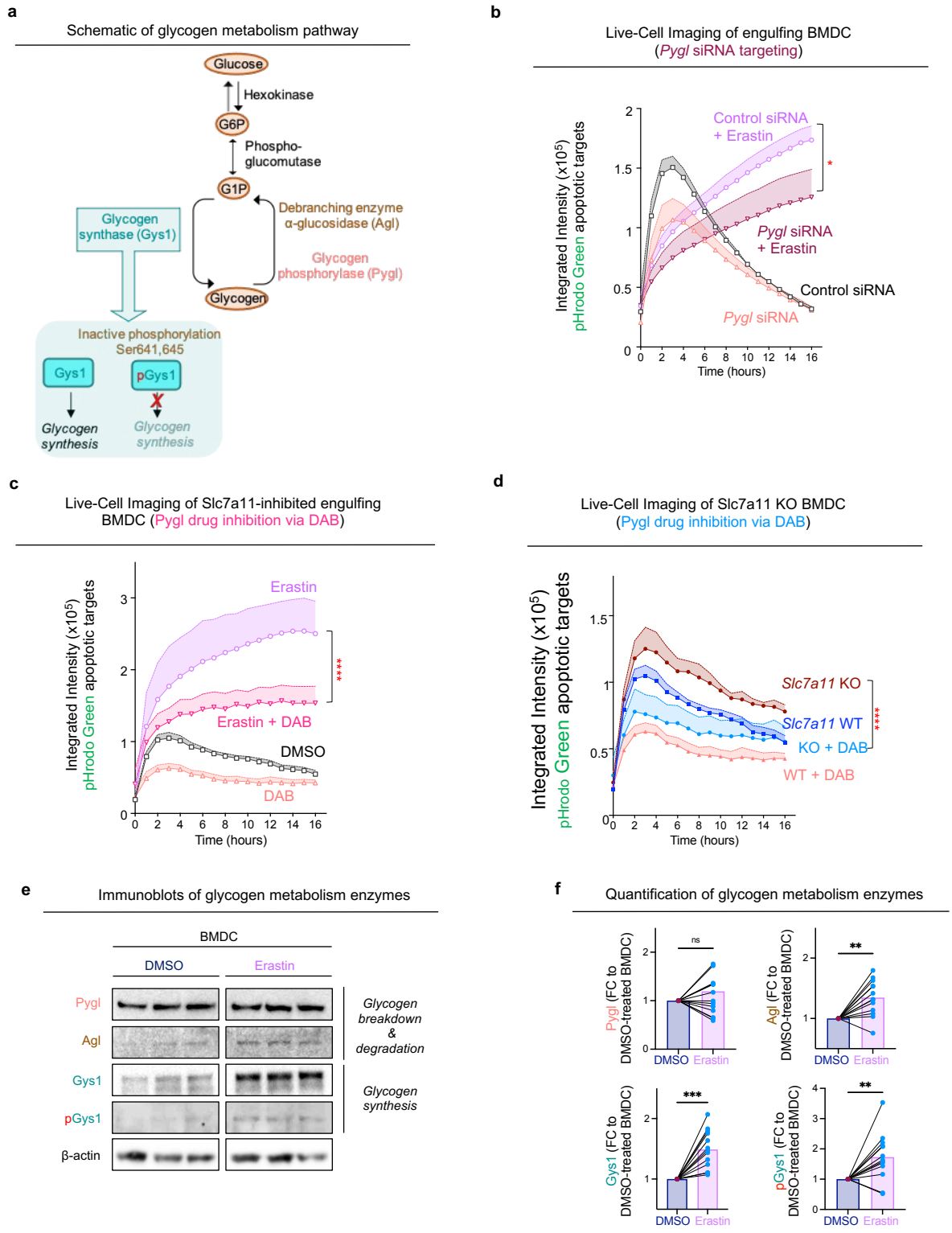


**Extended data Figure 6. Glycogen pools are altered in the absence of Slc7a11 and affect DC efferocytosis.**

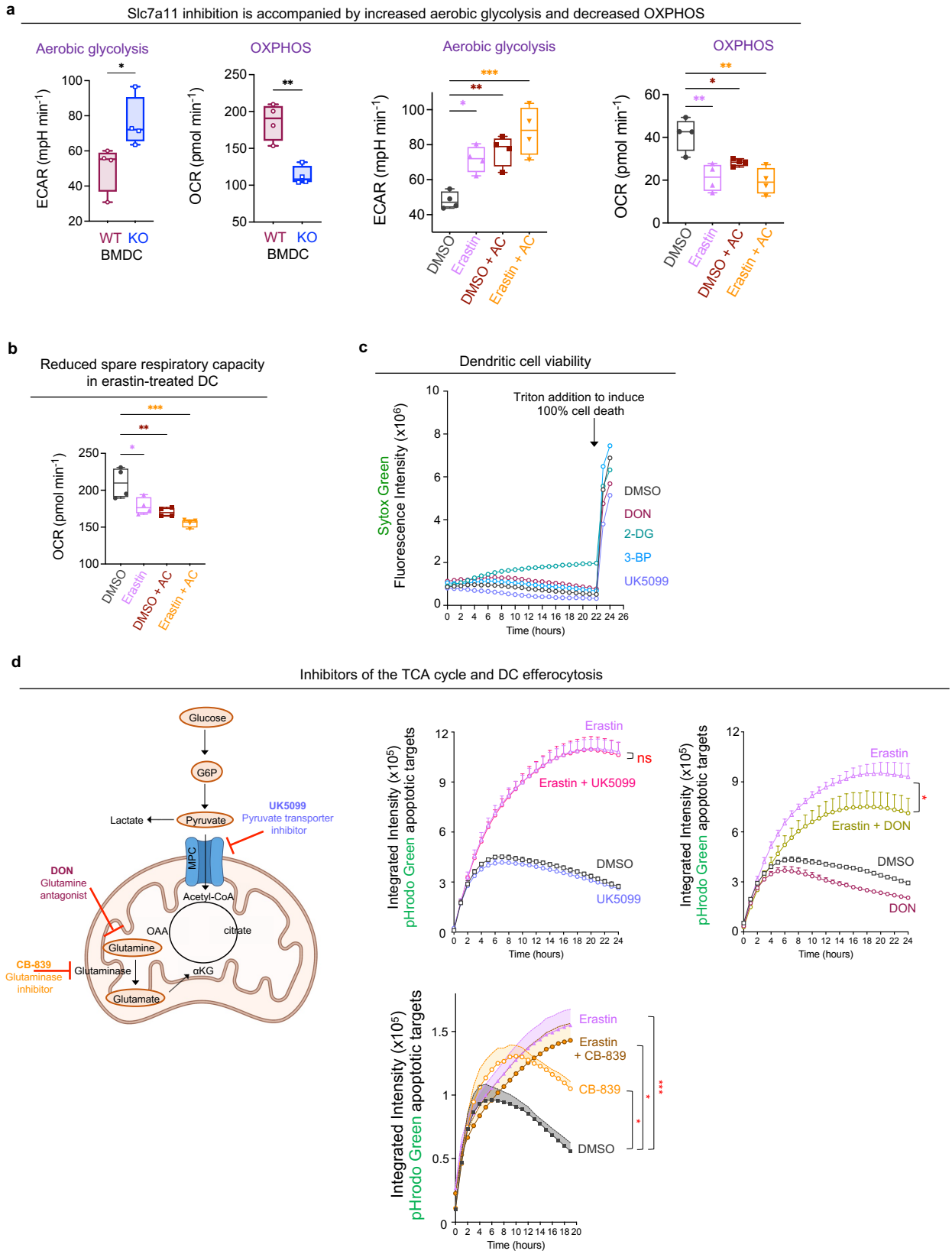


**Extended data Figure 7. Metabolic inhibitors and DC efferocytosis.**

**a**

Co-administration of CP-91149 or 3-BP with erastin regimen can rescue the accelerated wound healing in the context of Slc7a11 blockade.

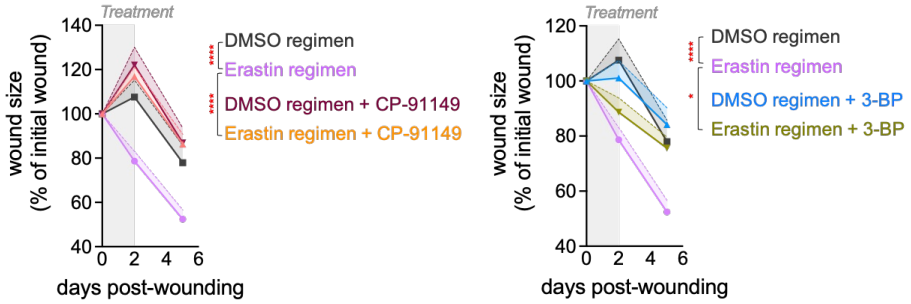


**Extended data Figure 8. Glycolysis/glycogen pathway inhibitors and wound healing.**

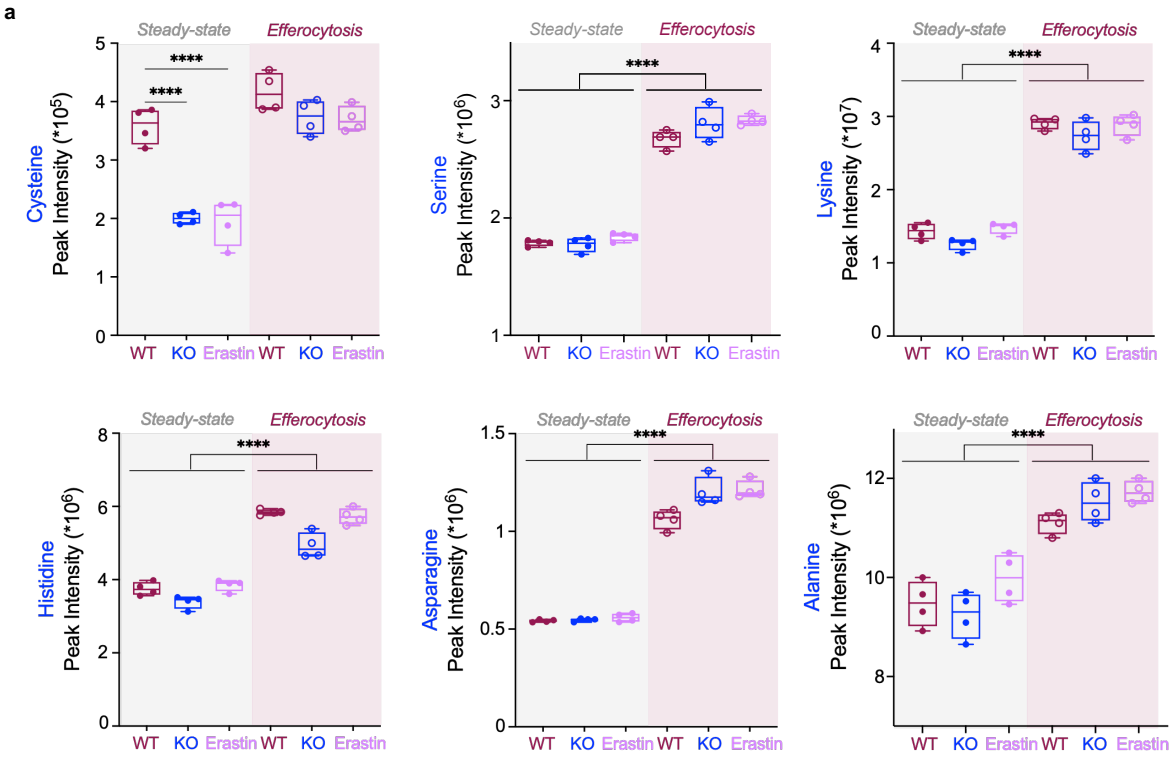


**Extended data Figure 9. Targeted metabolomics profiling in Slc7a11-null or inhibited DC.**

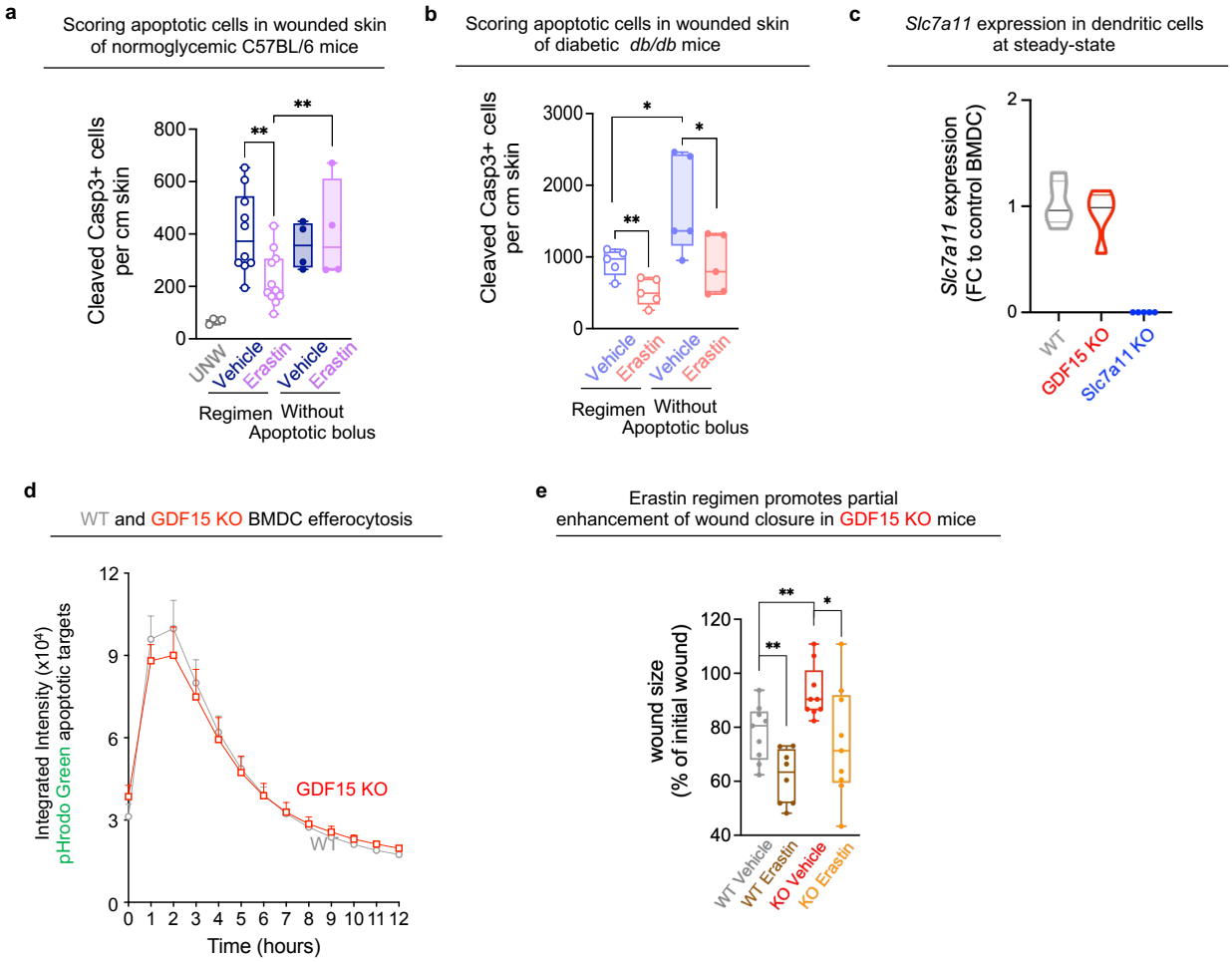


**Extended data 10. Erastin ameliorates corpse clearance in *db/db* wounds and promotes partial wound healing in GDF15KO mice.**

**Extended Data Table 1 | Top 10 predictions for Slc7a11 associated diseases via ARCHS[4].**

| Rank | Gene Set | Z-score |
|---|---|---|
| 1 | Eczematoid dermatitis (HP:0000976) | 8.37081035 |
| 2 | Recurrent abscesses formation (HP:0002722) | 8.33968455 |
| 3 | Recurrent bacterial skin infections (HP:0005406) | 7.83378133 |
| 4 | Recurrent gram-negative bacterial infections (HP:0005420) | 7.48198989 |
| 5 | Mediastinal lymphadenopathy (HP:0100721) | 6.49015299 |
| 6 | Abnormality of macrophages (HP:0004311) | 5.60196319 |
| 7 | Stomatitis (HP:0010280) | 5.37080502 |
| 8 | Gingivitis (HP:0000230) | 4.99950475 |
| 9 | Increased IgM level (HP:0003496) | 4.79775952 |
| 10 | Recurrent skin infections (HP:0001581) | 4.63188927 |

The predictions were derived from mining of publicly available RNA-seq data from human and mouse via ARCHS[4] database.